ATLAS CONF Note

ATLAS-CONF-2023-012

22nd March 2023

Measurements of W^+W^- production cross sections in pp collisions at $\sqrt{s} = 13$ TeV with the ATLAS detector

The ATLAS Collaboration

Measurements of $W^+W^- \to e^\pm\nu\mu^\mp\nu$ production cross-sections are presented, providing a test of the predictions of perturbative quantum chromodynamics, parton distribution functions, and the electroweak theory. The measurements are performed using pp collision data recorded by the ATLAS detector at the Large Hadron Collider in 2015–2018 at $\sqrt{s} = 13$ TeV, corresponding to an integrated luminosity of 140 fb^{-1}. The number of events due to top-quark pair production, the largest background, is reduced by rejecting events containing jets with b-hadron decays. An improved methodology of estimating the remaining top quark background enables a precise measurement of W^+W^- cross-sections with no additional requirements on jets. The fiducial W^+W^- cross section is determined in a maximum-likelihood fit with an uncertainty of 3.1%. The measurement is extrapolated to the full phase space, resulting in a total W^+W^- cross-section of 127 ± 4 pb. Differential cross-sections are measured as a function of twelve observables that comprehensively describe the kinematics of W^+W^- events. The measurements are compared to state-of-the art theory calculations and excellent agreement with predictions is observed.

ATLAS-CONF-2023-012
31 March 2023

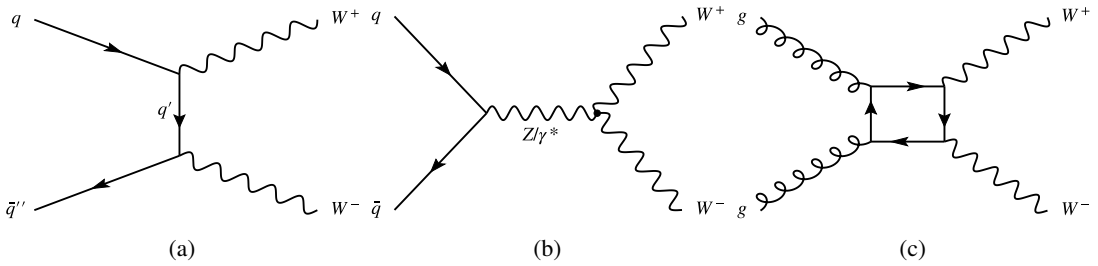

Figure 1: Illustrative examples of Feynman diagrams for (a) the t-channel and (b) s-channel $q\bar{q} \to WW$ as well as (c) the $gg \to WW$ production mechanisms of a WW pair.

1 Introduction

The measurement of W-boson pair (WW) production cross-sections is an important test of the Standard Model (SM). WW production at hadron colliders is sensitive to the properties of electroweak-boson self-interactions and provides a test of the predictions of perturbative quantum chromodynamics (QCD) and the electroweak (EW) theory. It also constitutes a large background in the measurement of Higgs boson production as well as in searches for physics beyond the SM. Inclusive and fiducial WW production cross-sections have been measured in proton–proton (pp) collisions at $\sqrt{s} = 5$ TeV [1], 7 TeV [2, 3], 8 TeV [4–6] and 13 TeV [7–11], as well as in e^+e^- collisions at LEP [12] and in $p\bar{p}$ collisions at the Tevatron [13–15].

Illustrative Feynman diagrams for WW production are shown in Figure 1. In pp collisions, the t-channel and s-channel of the $q\bar{q}$-induced WW production ($q\bar{q} \to WW$, shown on Figs 1(a) and 1(b) respectively) constitute most of the WW production rate with 95%. Loop-induced gluon–gluon fusion, $gg \to WW$ (Figure 1(c)), contributes 5%, despite formally being only a NNLO QCD correction to WW production. Beyond leading order in perturbation theory, additional partonic initial states can contribute to both $q\bar{q} \to WW$ and $gg \to WW$. Resonant $gg \to H \to WW$ production is included in the signal definition and simulation, although the process is strongly suppressed via the kinematic selection requirements of this analysis.

The measurement of integrated and differential $WW \to e^{\pm}\nu\mu^{\mp}\nu$ production cross-sections at $\sqrt{s} = 13$ TeV is performed using pp collision data recorded by the ATLAS experiment in 2015–2018, corresponding to an integrated luminosity of 140 fb^{-1} [16]. The number of events due to top-quark pair production ($t\bar{t}$), the largest background for this measurement, is reduced by rejecting events containing jets with b-hadron decays (b-jets). The di-lepton invariant mass is required to be greater than 85 GeV, to reduce the background due to Drell–Yan production of leptonically decaying tau lepton pairs.

The WW cross-section measurements are performed without any requirements on jets other than b-jets. This jet-inclusive measurement allows for the comparison with precise predictions in perturbative QCD that are not subject to large logarithmic corrections due to jet vetoes [17]. It is also advantageous from an experimental perspective as jet-related uncertainties are reduced.

Measurements of WW production are challenging due to the presence of a large top-quark pair production background. In contrast to previous ATLAS measurement [2, 4, 7, 8, 11], no jet veto or other selection requirements are employed to reduce this background. Instead the background contribution is precisely estimated with a data-driven method based on two control regions. The control regions allow for the

reduction of uncertainties arising in the theoretical modelling of top quark pairs and the efficiency of identifying b-jets. Backgrounds from W+jets events with a misidentified or non-prompt lepton, another large source of uncertainties in measurements of WW cross-sections, are estimated with a data-driven method while the remaining backgrounds are estimated based on theoretical calculations. For the determination of the integrated cross-section, a model based on these background estimates and a state-of-the-art signal model is fit to the data, further reducing uncertainties. Additionally, fiducial differential cross-sections of WW production are measured after background subtraction, using an iterative Bayesian unfolding method [92, 93]. Cross-sections are measured differentially as a function of:

- the transverse momentum[1] of the leading lepton[2], $p_{\mathrm{T}}^{\text{lead. lep.}}$,
- the transverse momentum of the sub-leading lepton, $p_{\mathrm{T}}^{\text{sub-lead. lep.}}$,
- the transverse momentum of the dilepton system, $p_{\mathrm{T},e\mu}$,
- the rapidity of the dilepton system, $y_{e\mu}$,
- the invariant mass of the lepton pair, $m_{e\mu}$,
- the azimuthal separation of the two leptons, $\Delta\phi_{e\mu}$,
- $\cos\theta^* = |\tanh(\Delta\eta_{e\mu}/2)|$, which is sensitive to the spin structure of the W-boson pair [18],
- the magnitude $E_{\mathrm{T}}^{\mathrm{miss}}$ of the missing transverse momentum $\vec{p}_{\mathrm{T}}^{\,\mathrm{miss}}$, defined as the negative vectorial sum of the transverse momenta of all visible particles,
- the scalar sum of $E_{\mathrm{T}}^{\mathrm{miss}}$ and the lepton transverse momenta, $H_{\mathrm{T}}^{\text{lep.+MET}}$,
- the transverse mass of the dilepton system and the missing transverse momentum[3], $m_{\mathrm{T},e\mu}$,
- the scalar sum of all jet and lepton transverse momenta, S_{T}, and
- the jet multiplicity.

This note is organized as follows. Section 2 gives a brief overview of the ATLAS detector. The recorded data set and the simulated samples used are listed in Section 3. The criteria required to define object and event selection in the signal region are given in Section 4. Section 5 presents the estimates for top-quark (Section 5.1) and non-prompt lepton (Section 5.2) backgrounds, Drell-Yan (Section 5.3) and other backgrounds (Section 5.4), as well as a summary of the selected WW candidate events (Section 5.5). The statistical analysis to determine fiducial and differential cross-sections is presented in Section 6, while Section 7 contains the systematic uncertainties considered and their treatment. Measurement of fiducial cross-sections, both integrated and differential distributions, are compared to state-of-the-art predictions described in Section 8. Section 9 reports the results of the measurement for fiducial and total cross-sections. The note ends with the drawn conclusions in Section 10.

[1] ATLAS uses a right-handed coordinate system with its origin at the nominal interaction point (IP) in the centre of the detector and the z-axis along the beam pipe. The x-axis points from the IP to the centre of the LHC ring, and the y-axis points upwards. Cylindrical coordinates (r, ϕ) are used in the transverse plane, ϕ being the azimuthal angle around the z-axis. The rapidity is defined as $y = \frac{1}{2}\ln\frac{E+p_z}{E-p_z}$ while the pseudorapidity is defined in terms of the polar angle θ as $\eta = -\ln\tan(\theta/2)$. Angular distance is measured in units of $\Delta R \equiv \sqrt{(\Delta\eta)^2 + (\Delta\phi)^2}$.

[2] The lepton with (second) highest p_{T} in the event is referred to as (sub-)leading lepton.

[3] The transverse mass is defined as $m_{\mathrm{T},e\mu} = \sqrt{(E_{\mathrm{T},e\mu} + E_{\mathrm{T}}^{\mathrm{miss}})^2 - (\vec{p}_{\mathrm{T},e\mu} + \vec{p}_{\mathrm{T}}^{\,\mathrm{miss}})^2}$, where $E_{\mathrm{T},e\mu} = \sqrt{|\vec{p}_{\mathrm{T},e\mu}|^2 + m_{e\mu}^2}$.

2 The ATLAS detector

The ATLAS experiment [19] at the LHC [20] is a multipurpose particle detector with a forward–backward symmetric cylindrical geometry and a near 4π coverage in solid angle. It consists of an inner tracking detector surrounded by a thin superconducting solenoid providing a 2 T axial magnetic field, electromagnetic and hadron calorimeters, and a muon spectrometer with three large superconducting toroidal magnets with eight coils each.

The inner tracking detector (ID) covers the pseudorapidity range $|\eta| < 2.5$. It consists of a high-granularity silicon pixel detector, including the insertable B-layer installed before Run 2 [21, 22], followed by the silicon microstrip tracker. The silicon detectors are complemented by a transition radiation tracking detector, enabling extended track reconstruction within $|\eta| < 2.0$.

Lead/liquid-argon (LAr) sampling calorimeters provide electromagnetic (EM) energy measurements with high granularity. A steel/scintillator-tile hadron calorimeter covers the central pseudorapidity range ($|\eta| < 1.7$). The endcap and forward regions are instrumented with copper/LAr and tungsten/LAr calorimeters for EM and hadronic energy measurements up to $|\eta| = 4.9$.

The muon spectrometer surrounds the calorimeters and is based on three large air-core toroidal superconducting magnets with eight coils each. The field integral of the toroids ranges between 2.0 and 6.0 Tm across most of the detector. The muon spectrometer includes a system of precision tracking chambers and fast detectors for triggering.

Events are selected using a two-level trigger system. The first-level trigger is implemented in hardware and uses a subset of the detector information to accept events at a rate of about 100 kHz. The level-1 trigger is followed by a software-based trigger that reduces the accepted event rate to 1 kHz on average depending on the data-taking conditions.

An extensive software suite [23] is used in data simulation, in the reconstruction and analysis of real and simulated data, in detector operations, and in the trigger and data acquisition systems of the experiment.

3 Data and Monte Carlo samples

The analysis uses data collected in proton–proton collisions at a centre-of-mass energy of 13 TeV from 2015 to 2018. After applying data quality criteria [24], the dataset corresponds to 140 fb^{-1} of integrated luminosity, with an uncertainty of 0.83% [16], obtained using the LUCID-2 detector [25] for the primary luminosity measurements.

Monte Carlo (MC) simulated event samples are used to correct the signal yield for detector effects and to estimate background contributions. All samples were passed through a full simulation of the ATLAS detector [26], based on GEANT4 [27]. Table 1 lists the configurations for the nominal MC simulations used in the analysis.

Signal $q\bar{q} \to WW$ events are modelled using POWHEG MiNNLO [28, 29], which is next-to-next-to-leading order (NNLO) accurate in QCD for inclusive observables. The aforementioned signal sample and all other WW production processes described in the following were generated using the NNPDF3.0NNLO PDF set [30]. The events were interfaced to PYTHIA 8.245 [31] for the modelling of the parton shower, hadronization, and underlying event, with parameters set according to the A14 tune [46]. The matrix element calculation of

Table 1: Summary of the nominal Monte Carlo simulated samples used in the analysis. The $gg \to WW$ simulation includes Higgs boson contributions. The last two columns give the order in α_S of the matrix element calculation and the overall cross-section normalization. All nominal MC samples use the NNPDF3.0 PDF set. The samples generated with SHERPA use its default set of tuned parton-shower parameters, while for the POWHEG BOX samples the A14 set of tuned parameters and the NNPDF2.3LO PDF set are used for the parton shower.

Process	Generator	Parton shower	Matrix element $O(\alpha_S)$	Normalization
$q\bar{q} \to WW$	MINNLO	PYTHIA8	NNLO	Generator
$gg \to WW$	SHERPA2.2.2	SHERPA	LO (0–1 jet)	NLO
$t\bar{t}$	POWHEG BOXV2	PYTHIA8	NLO	NNLO+NNLL
Wt	POWHEG BOXV2	PYTHIA8	NLO	NLO+NNLL
Z+jets	SHERPA2.2.1	SHERPA	NLO (0–2 jets), LO (3–4 jets)	NNLO
WZ, ZZ	SHERPA2.2.2	SHERPA	NLO (0–1 jet), LO (2–3 jets)	Generator†
$W\gamma, Z\gamma$	SHERPA2.2.8	SHERPA	NLO (0–1 jet), LO (2–3 jets)	Generator†

†: The cross-section calculated by SHERPA is found to be in good agreement with the NNLO result [67–71].

$gg \to WW$ production, which includes off-shell effects and Higgs boson contributions, incorporates up to one additional parton emission at LO. This contribution was simulated with the SHERPA2.2.2 [32, 33] generator, which was matched and merged with the SHERPA parton shower based on the Catani–Seymour dipole [34, 35] using the MEPS@NLO prescription [36–39]. The virtual QCD corrections were provided by the OPENLOOPS library [40, 41]. The electroweak production of a diboson in association with two jets ($VVjj$) was simulated with the SHERPA 2.2.2 [32] generator. The LO-accurate matrix elements were also matched to a parton shower based on Catani–Seymour dipole factorization [34, 35] using the MEPS@LO prescription [36–39]. A dedicated set of tuned parton-shower parameters developed by the SHERPA authors was used for all SHERPA samples.

The production of $t\bar{t}$ and single-top Wt events are modelled using the POWHEG BOXV2 [42–45] generator at NLO with the NNPDF3.0NLO [30] PDF. The events were interfaced to PYTHIA8.230 [31] to model the parton shower, hadronization, and underlying event, with the A14 set of tuned parameters [46] and using the NNPDF2.3LO set of PDFs [47]. For $t\bar{t}$ event generation, the h_{damp} parameter[4] was set to $1.5m_{\text{top}}$ [48]. The diagram-removal scheme [49] was employed to handle the interference between the Wt and $t\bar{t}$ production processes [48]. Alternative samples were generated to assess the uncertainties in the top-background modelling. The uncertainty due to initial-state radiation and higher-order QCD effects was estimated by simultaneous variations of the h_{damp} parameter and the renormalization and factorization scales, and by choosing the VAR3c up/down variants of the A14 set of tuned parameters, corresponding to the varying of α_s in the parton shower, as described in Ref. [50]. The impact of final-state radiation was evaluated with weights that account for the effect of varying the renormalization scale for final-state parton-shower emissions up or down by a factor of two. To assess the dependence on the $t\bar{t}$–Wt overlap removal scheme, the diagram-subtraction scheme [49] was employed as an alternative to the diagram-removal scheme. The uncertainty due to the parton shower and hadronization model was evaluated by comparing the nominal sample of events with an event sample generated by POWHEG BOXV2 and interfaced to HERWIG7.04 [51, 52], using the H7UE set of tuned parameters [52] and the MMHT2014LO PDF set [53]. To estimate the uncertainty in the matching of NLO matrix elements to the parton shower, the nominal sample was compared with a sample generated by MADGRAPH5_AMC@NLO2.6.2 [54] at NLO in QCD using the

[4] The h_{damp} parameter is a resummation damping factor and one of the parameters that control the matching of POWHEG matrix elements to the parton shower and thus effectively regulates the high-p_T radiation against which the $t\bar{t}$ system recoils.

five-flavour scheme and the NNPDF2.3NLO PDF set. The events were interfaced with PYTHIA8, as for the nominal sample. The $t\bar{t}$ sample was normalized to the cross-section prediction at NNLO in QCD including the resummation of next-to-next-to-leading logarithmic (NNLL) soft-gluon terms calculated using TOP++2.0 [55–61]. The inclusive cross-section for single-top Wt was corrected to the theory prediction calculated at NLO in QCD with NNLL soft-gluon corrections [62, 63].

The background due to Z/γ^*+jets production was simulated with the SHERPA2.2.1 generator using NLO-accurate matrix elements for up to two jets, and LO-accurate matrix elements for three and four jets calculated with the Comix [34] and OPENLOOPS libraries. They were matched with the SHERPA parton shower [35] using the MEPS@NLO prescription [36–39] and the set of tuned parameters developed by the SHERPA authors. The NNPDF3.0NNLO set of PDFs was used, and the samples were normalized to a NNLO prediction [64].

The production of diboson final states was simulated with the SHERPA2.2.2 (WZ, ZZ with $V = W, Z$) and SHERPA2.2.8 ($V\gamma$) generators using OPENLOOPS at NLO QCD accuracy for up to one additional parton and LO accuracy for two to three additional parton emissions, matched and merged with the SHERPA parton shower. The VZ simulation includes $V\gamma^*$ contributions for $m(\ell\ell) > 4\,\text{GeV}$. Samples were generated using the NNPDF3.0NNLO PDF set and normalized to the cross-section calculated by the event generator.

Samples generated with POWHEG BOX or MADGRAPH5_AMC@NLO used the EVTGEN program [65] to model the decay of bottom and charm hadrons. The effect of multiple interactions in the same and neighbouring bunch crossings (pile-up) was modelled by overlaying the hard-scattering event with simulated inelastic pp events generated with PYTHIA8.186 using the NNPDF2.3LO set of PDFs and the A3 set of tuned parameters [66].

4 Event reconstruction and selection

Candidate WW events are selected by requiring exactly one electron and one muon with opposite electric charges. These leptons are required to be isolated, i.e., there should be little hadronic activity in the vicinity of the lepton, to suppress backgrounds due to misidentified leptons or leptons from hadron decays. Events with two isolated leptons of the same flavour are not considered in the analysis due to the higher background from Drell–Yan events.

Events were recorded by either single-electron or single-muon triggers. The minimum p_{T} threshold varied during data-taking between 24 GeV and 26 GeV for electrons, and between 20 GeV and 26 GeV for muons, both requiring 'loose' to 'medium' isolation criteria [72, 73]. Triggers with higher p_{T} thresholds and looser isolation requirements are also used to increase the efficiency. The trigger selection efficiency is more than 99% for signal events fulfilling all other selection requirements detailed in the following.

Trajectories of charged particles are reconstructed as tracks in the ID, whose common vertices are used to extract interaction vertex candidates. Candidate events are required to have at least one vertex having at least two associated tracks with $p_{\text{T}} > 500\,\text{MeV}$. The vertex with the highest $\sum p_{\text{T}}^2$ of the associated tracks is taken as the primary vertex.

Electrons are reconstructed from energy deposits in the calorimeter that are matched to tracks [74]. Electron candidates are required to fulfil the `TightLH` likelihood-based identification criteria as defined in Ref. [75]. Furthermore, they are required to have $E_{\text{T}} > 27\,\text{GeV}$ and $|\eta| < 2.47$, excluding the transition region between barrel and endcap regions, $1.37 < |\eta| < 1.52$.

Muon candidates are reconstructed by combining a track in the inner detector with a track in the muon spectrometer [76]. Muons are required to have $p_{\mathrm{T}} > 27\,\mathrm{GeV}$ and $|\eta| < 2.5$ and to satisfy the `Medium` identification selection, as defined in Ref. [76].

Leptons are required to be compatible with the primary vertex by imposing requirements on the impact parameters of associated tracks. The transverse impact parameter significance, d_0/σ_{d_0}, is required to satisfy $|d_0/\sigma_{d_0}| < 5\,(3)$ for electrons (muons). The longitudinal impact parameter z_0 must satisfy $|z_0 \cdot \sin\theta| < 0.5\,\mathrm{mm}$, where θ is the polar angle of the track. Additionally, leptons are required to be isolated using information from the ID tracks and energy clusters in the calorimeters in a cone around the lepton. The `Gradient` working point is used for electrons [75], while for muons the `Tight_FixedRad` working point is used, which is similar to the `Tight` selection defined in Ref. [77] but with altered criteria at muon $p_{\mathrm{T}} > 50\,\mathrm{GeV}$ in order to increase the background rejection. The electron or muon trigger object is required to match the respective reconstructed lepton.

Jets are reconstructed using the anti-k_t algorithm [78] with a radius parameter of $R = 0.4$ using particle-flow objects [79]. They are required to have $p_{\mathrm{T}} > 30\,\mathrm{GeV}$ and $|\eta| < 4.5$. To suppress jets that originate from pile-up, a jet-vertex tagger [80] is applied to jets with $p_{\mathrm{T}} < 60\,\mathrm{GeV}$ and $|\eta| < 2.4$. The jet energy scale is recalibrated using a η- and p_{T} correction [81]. Jets with $p_{\mathrm{T}} > 20\,\mathrm{GeV}$ and $|\eta| < 2.5$ containing decay products of a b-hadron are identified using the DL1r b-tagging algorithm [82, 83] at the 85% efficiency working point. Selecting b-jets with a lower p_{T} threshold enables the rejection of a larger fraction of the $t\bar{t}$ background.

In order to resolve the overlap between particles reconstructed as multiple physics objects in the detector, non-b-tagged jets are removed if they overlap, within $\Delta R < 0.2$, with an electron, or with a muon if the jet has less than three associated tracks with $p_{\mathrm{T}} > 500\,\mathrm{MeV}$ and satisfies $p_{\mathrm{T}}^{\mu}/p_{\mathrm{T}}^{\mathrm{jet}} > 0.5$, and the ratio of the muon p_{T} to the sum of the track p_{T} associated with the jet is greater than 0.7. After the former selection, electrons or muons overlapping within $\Delta R < 0.4$ with any jet, including b-tagged jets, are removed.

The missing transverse momentum, with magnitude $E_{\mathrm{T}}^{\mathrm{miss}}$, is computed as the negative vectorial sum of the transverse momenta of tracks associated with jets and muons, as well as tracks in the ID that are not associated with any other component. The p_{T} of the electron track is replaced by the calibrated transverse momentum of the reconstructed electron [84].

Events with one or more b-tagged jets are vetoed, to reduce the dominant background from top-quark pair production. To reduce the Drell–Yan backgrounds, dominated by Z+jets events with $Z \to \tau^+\tau^-$ decays, the invariant mass of the electron–muon pair is required to be $m_{e\mu} > 85\,\mathrm{GeV}$. This requirement also reduces the contribution of resonant $gg \to H \to WW$ production. Events with additional leptons with $p_{\mathrm{T}} > 10\,\mathrm{GeV}$ and satisfying `Loose` isolation and `LooseLH` (`Loose`) identification requirements for electrons (muons), are vetoed to reduce backgrounds due to WZ and ZZ production.

Table 2 gives a summary of the lepton, jet, and event selection requirements used to define the signal region.

5 Background estimate

About 60% of the events passing the event selection are background events. The top-quark background, from either $t\bar{t}$ or single-top Wt production, is the largest background and comprises about 80% of the

Table 2: Summary of the object and event selection criteria.

Selection	Criteria
Lepton p_{T}	> 27 GeV
Lepton η	$\lvert\eta\rvert < 2.47$ and not $1.37 < \lvert\eta\rvert < 1.52$ (electron) $\lvert\eta\rvert < 2.5$ (muon)
Lepton identification	`TightLH` (electron), `Medium` (muon)
Lepton isolation	`Gradient` (electron), `Tight_FixedRad` (muon)
Lepton impact parameter	$\lvert d_0/\sigma_{d_0}\rvert < 5, 3$ (electron, muon) $\lvert z_0 \cdot \sin\theta\rvert < 0.5$ mm
b-jet selection	$p_{\mathrm{T}} > 20$ GeV, $\lvert\eta\rvert < 2.5$, DL1r (85% eff. WP)
Jet selection	$p_{\mathrm{T}} > 30$ GeV, $\lvert\eta\rvert < 4.5$
Lepton selection	1 electron and 1 muon of opposite charge, no additional lepton with $p_{\mathrm{T}} > 10$ GeV, `Loose` isolation, and `LooseLH` (electron) / `Loose` (muon) identification
Number of b-jets	0
Dilepton invariant mass	> 85 GeV

total background. Additional backgrounds considered are Z+jets production, events with non-prompt or misidentified leptons, and diboson production (WZ, $W\gamma$, ZZ, and $Z\gamma$).

5.1 Top-quark background

An estimate of the $t\bar{t}$ background is obtained using a data-driven technique referred to as the b-tag counting method, performed in each individual bin for the differential measurements. Following the procedure used in a measurement of the $t\bar{t}$ production cross-section [85] and in the measurement of WW+jets production [10], two control regions requiring exactly one and exactly two b-tagged jets are defined. All other selection criteria are the same as in the signal region. The contribution of non-$t\bar{t}$ events in the 1-b-jet and 2-b-jet control regions is 13% and 4% of the expected events, respectively, of which 90% can be attributed to single-top Wt production.

The number of $t\bar{t}$ events in the two control regions and the signal region, after subtracting non-$t\bar{t}$ backgrounds, is parametrized using three parameters. The first is the number of $t\bar{t}$ events without requirements on the b-jet multiplicity, $N^{t\bar{t}}_{\geq 0b}$. The second is the efficiency of identifying and selecting a b-jet in a $t\bar{t}$ event, ε_b, accounting for the efficiency of the b-tagging algorithm as well as the acceptance of b-jets. The third is the b-jet correlation factor C_b, which takes into account that the probability of identifying both b-jets in a $t\bar{t}$ events is not exactly ε_b^2 but $C_b\varepsilon_b^2$, due to correlation effects that depend on the interplay of event selection and $t\bar{t}$ kinematics as well as the presence of additional light jets and b-jets. The number of $t\bar{t}$ events with exactly i b-tagged jets, $N^{t\bar{t}}_{ib}$, is given by

$$N^{t\bar{t}}_{2b} = N^{t\bar{t}}_{\geq 0b} \cdot C_b\varepsilon_b^2 \,, \tag{1}$$

$$N^{t\bar{t}}_{1b} = N^{t\bar{t}}_{\geq 0b} \cdot \left(2\varepsilon_b - C_b\varepsilon_b^2\right) \,, \tag{2}$$

$$N^{t\bar{t}}_{0b} = N^{t\bar{t}}_{\geq 0b} \cdot \left(1 - 2\varepsilon_b + C_b\varepsilon_b^2\right) \,. \tag{3}$$

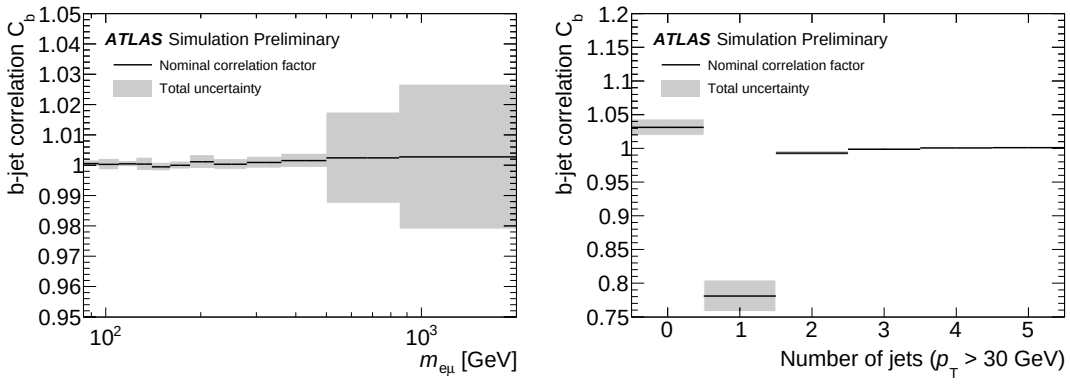

(a) (b)

Figure 2: The b-jet correlation correction factor C_b as evaluated from simulation as a function of (a) $m_{e\mu}$ and (b) the number of jets. The error bands show the total uncertainty, including systematic effects.

Using these equations, the number of $t\bar{t}$ events in the signal region can be expressed as

$$N_{0b}^{t\bar{t}} = \frac{C_b}{4} \frac{\left(N_{1b}^{t\bar{t}} + 2N_{2b}^{t\bar{t}}\right)^2}{N_{2b}^{t\bar{t}}} - N_{1b}^{t\bar{t}} - N_{2b}^{t\bar{t}} \,, \tag{4}$$

where the only input from $t\bar{t}$ simulation is C_b while ε_b and $N_{\geq 0b}^{t\bar{t}}$ are determined by the observed yields in the two control regions.

The correction factor C_b is typically close to unity, between 0.99 and 1.01 across jet-inclusive distributions, like $m_{e\mu}$ (Figure 2(a)). As uncertainties in top modelling and b-tagging primarily affect ε_b and $N_{\geq 0b}^{t\bar{t}}$ but not C_b, the uncertainty in C_b is less than 1% in most analysis bins. In certain configurations, for example in events with exactly one jet with $p_{\mathrm{T}} > 30\,\mathrm{GeV}$, C_b can be as low as 0.8 (Figure 2(b)). The identification of two b-jets is possible for some of these events, as the b-jet p_{T} requirement is 20 GeV. However, the probability of identifying both b-jets is significantly smaller than ε_b^2 as the second jet is often outside the acceptance and because the b-tagging efficiency is lower for jets with a transverse momentum between 20 GeV and 30 GeV. The disparity in jet kinematics thus leads to smaller values of C_b while the reduced correlation of the uncertainties of finding the first and the second jet increases the uncertainty in C_b.

The b-jet counting method strongly reduces experimental and theoretical uncertainties in the $t\bar{t}$ background estimate, and thus lowers its total uncertainty by a factor of approximately five, corresponding to an uncertainty of about 3%.

The single-top Wt background is estimated using simulation. The subtraction of Wt backgrounds in the $t\bar{t}$ control regions introduces an anti-correlation in the estimated Wt and $t\bar{t}$ yield in the signal region so that modelling uncertainties in Wt have a reduced impact on the measurement.

In a few analysis bins, the two-b-jet control region contains relatively few events, which would result in a large statistical uncertainty of the $t\bar{t}$ background estimate. To mitigate this problem, the top-quark background is instead estimated with the transfer-factor method in these bins, by extrapolating from a control region constructed by requiring at least one b-jet, with other selection criteria being the same as in the signal region. For each bin of the measured distribution in the signal region, the number of expected

top-quark background events from both $t\bar{t}$ and Wt contributions, $N_{\mathrm{SR}}^{\mathrm{top}}$, is estimated from the corresponding bin in the control region as

$$N_{\mathrm{SR}}^{\mathrm{top}} = \frac{N_{\mathrm{SR}}^{\mathrm{top,MC}}}{N_{\mathrm{CR}}^{\mathrm{top,MC}}} \times \left(N_{\mathrm{CR}}^{\mathrm{data}} - N_{\mathrm{CR}}^{\mathrm{MC,others}} \right) . \tag{5}$$

Here $N_{\mathrm{CR}}^{\mathrm{MC,others}}$ is the contribution from non-top background in the control region, which is of the order of 10% of the total and estimated from MC simulation. The transfer factor, $\frac{N_{\mathrm{SR}}^{\mathrm{top,MC}}}{N_{\mathrm{CR}}^{\mathrm{top,MC}}}$, is defined as the ratio of events expected in the signal and control regions and also estimated from MC simulation. It has an uncertainty of about 10%. Therefore, the transfer factor method is only employed in a few bins at the high-mass tails ($m_{e\mu} \gtrsim 0.5$ TeV) of the distributions where there are fewer than 100 events in the two-b-jet region, as its uncertainty is smaller than the uncertainty of the b-tag counting method in these bins. The effect of experimental and theory uncertainties is reduced compared to a background estimate purely based on simulation. The dominant uncertainties arise in the theoretical modelling of the top-quark background.

The top-quark background estimate is validated in a top-enriched region that overlaps with the signal regions, by requiring at least one jet and $m_{\ell j} < 140$ GeV as well as $\Delta\phi_{e\mu} < \pi/2$ in addition to the normal event selection. Here $m_{\ell j}$ is the invariant mass of the leading jet and the closest lepton. This region is approximately 70% pure in top events and shows good agreement between the data and the combined signal and background prediction, which uses the data-driven top-quark background estimate.

Figs. 3(a) and 3(b) show the distributions of the $p_{\mathrm{T}}^{\text{lead. lep.}}$ and the jet multiplicity, confirming the accurate modelling of lepton and jet-related properties in events without b-jets.

5.2 Backgrounds with non-prompt or misidentified leptons

Reducible backgrounds from events with non-prompt or misidentified leptons are called fake-lepton backgrounds or "fakes". Fake leptons correspond to leptons from heavy-flavour hadron decays and jets misidentified as electrons. Fake-lepton events stem mainly from W+jets production and contribute about 4% of the selected events.

Fake-lepton backgrounds are estimated using a data-driven technique. A control region is defined, where one of the two lepton candidates fails the nominal selection, but instead fulfils a looser set of requirements, designed to increase the contribution of fake leptons. The lepton failing the nominal selection is required to fulfil a loose (instead of a tight) isolation requirement and either, in the case of an electron, the medium (instead of tight) identification criteria or, in the case of a muon, an impact parameter significance requirement of $|d_0/\sigma_{d_0}| < 10$ (instead of $|d_0/\sigma_{d_0}| < 3$).

The fake-lepton background in the signal region is, then, obtained by scaling the number of data events in this control region by an extrapolation factor, after subtracting processes with two prompt leptons using simulation. The extrapolation factor from the control to the signal region is determined in a data sample that is dominated by fake leptons, and it depends on the p_{T}, $|\eta|$, and flavour of the lepton. The data sample is selected by requiring events with a dijet-like configuration with one lepton candidate recoiling against a jet, with $|\Delta\phi_{\ell j}| > 2.8$. To suppress contamination from W+jets events in this sample, the sum of $E_{\mathrm{T}}^{\mathrm{miss}}$ and the transverse mass of the lepton and $E_{\mathrm{T}}^{\mathrm{miss}}$ system is required to be smaller than 50 GeV. The extrapolation factor is determined as the number of events with a lepton fulfilling the nominal selection requirements divided by the number of events with a lepton fulfilling only the looser set of requirements. Systematic

uncertainties in the composition of the different sources of fake leptons are estimated by varying the selection of the data sample in which the extrapolation factors are determined. The variations include selecting events with a b-jet recoiling against the lepton candidate, selecting only events without b-jet, as well as changing the $E_{\mathrm{T}}^{\mathrm{miss}}$ requirements to increase the fake-lepton contributions.

Events with two prompt leptons (including electrons or muons from prompt tau decays) constitute about 75% of the event yield in the control region, as the looser event selection requirements are relatively similar to the signal region requirements, to ensure fake leptons originate from similar sources in both regions. Hence this prompt lepton yield needs to be determined exactly to facilitate a precise fake lepton estimate, as detailed in the following. The probability of prompt leptons to fulfil the loose but not the tight set of requirements is determined in control regions dominated by on-shell Z boson production. Same flavour events are selected to derive corrections for prompt electrons and muons while different flavour events are used to derive corrections for leptons from the decay of prompt taus. Correction factors depending on p_{T}, $|\eta|$, lepton flavour, and parton shower model are determined and used to correct the number of simulated events with two prompt leptons in the control region. The dominant uncertainties of this procedure cover the dependence of the correction factors on the hadronic activity in the event and on different periods of data taking. Systematic uncertainties other than those associated with lepton identification are treated as fully correlated with the signal region, which reduces the total uncertainty in the signal region as it introduces an anti-correlation between prompt and fake-lepton backgrounds. The signal contamination in the control region is subtracted using the WW simulation, corrected in each bin by the ratio of background subtracted data and WW simulation in the signal region. The uncertainty on the correction factor is taken to be 5%, which covers uncertainties in the signal subtraction in bins in which the fake-lepton background constitutes a relevant contribution to the total event yield.

The total relative uncertainty in the fake-lepton background is about 25%.

In order to validate the estimate of the fake-lepton background, the opposite-charge requirement of the signal region selection is inverted, and events with an electron–muon pair of the same charge are selected. This selection increases the contribution of W+jets events to about 25% after suppressing prompt lepton processes strongly, which are mostly charge asymmetric. The modelling of the fake-lepton background can be validated despite the relatively low purity since the dominant diboson background in this region is known with a precision of about 10%. Good agreement of the prediction with the data is observed, as is shown for the $p_{\mathrm{T}}^{\text{sub-lead. lep.}}$ distribution in Figure 3(c) .

5.3 Drell–Yan background

The Drell–Yan Z+jets background is estimated using MC simulation. The $m_{e\mu} > 85$ GeV requirement strongly suppresses this background. The contribution of this background to the selected events in the signal region is about 5%, almost entirely due to $Z/\gamma^* \to \tau^+\tau^-$+jets events.

The Z+jets estimate is checked in a validation region requiring a dilepton invariant mass between 45 GeV and 80 GeV and either $p_{\mathrm{T},e\mu} < 30$ GeV or $E_{\mathrm{T}}^{\mathrm{miss}} < 20$ GeV, in addition to the b-jet veto. The Z+jets purity of this region is about 85% and good modelling of the data is observed. Figure 3(d) shows the distribution of the dilepton invariant mass $m_{e\mu}$ in the validation region, which features the resonant $Z \to \tau\tau$ distribution over a rising background of top events.

Table 3: Selected WW candidate events in data, together with the signal prediction and the background estimates. The uncertainties include statistical and systematic contributions, excluding theory uncertainties on the signal. The fractions in percent give the relative contribution to the total SM prediction. The individual uncertainties are correlated, and do not add up in quadrature to the total uncertainty.

Category	Event yield	
Data	144221	
Total SM	139700 ± 2400	
WW	56900 ± 1100	41%
Total bkg.	82600 ± 2100	59%
Top	66500 ± 1900	48%
Drell-Yan	6500 ± 400	5%
Fakes	5000 ± 1300	4%
WZ,ZZ,$V\gamma$	4500 ± 600	3%

In addition to the theoretical uncertainty in the Z+jets cross-section of 5% [86], uncertainties in the Z+jets background are estimated by varying the renormalization and factorization scales used in the matrix element calculation by factors of two, avoiding variations in opposite directions.

5.4 Other backgrounds

Backgrounds from WZ, ZZ, $W\gamma$ and $Z\gamma$ production are estimated from simulation, and are found to contribute about 4% of the total selected events. The dominant contribution are WZ events, which are observed to be well described by the nominal SHERPA simulation in Ref. [87]. Uncertainties due to missing higher-order QCD corrections are derived by varying the factorization and renormalization scales used in the matrix element calculations by factors of two, avoiding variations in opposite directions. Additionally, the uncertainty in the diboson cross-section of 10% [88, 89] is included.

The VZ (WZ and ZZ) prediction is validated in events containing a third lepton having $p_{\mathrm{T}} \geq 10\,\mathrm{GeV}$ that must satisfy loosened identification criteria. The invariant mass of the resulting same-flavour opposite-charge pair of leptons is required to be between 80 GeV and 100 GeV, close to the Z-boson mass while the remaining selection criteria are identical to the signal region. These selections give a very pure sample of diboson events, and the prediction is in good agreement with the data, as seen in Figure 4(a), where the $E_{\mathrm{T}}^{\mathrm{miss}}$ distribution in the VZ validation region shows separation between ZZ and WZ events.

$V\gamma$ ($W\gamma$ and $Z\gamma$) events enter the signal region as backgrounds when the photon is reconstructed and selected as an electron candidate. To validate estimates of these backgrounds, the electron identification requirements are changed such that contributions from photon conversions increase. As the electron candidates reconstructed from photon conversion are charge symmetric, both opposite-charge and same-charge candidates are selected with respect to the selected muon. For the $V\gamma$ validation region the p_{T} distribution of the electron candidates is shown in Figure 4(b). It is dominated by electrons from photon conversion. Excellent agreement with the observed data in the validation regions is found.

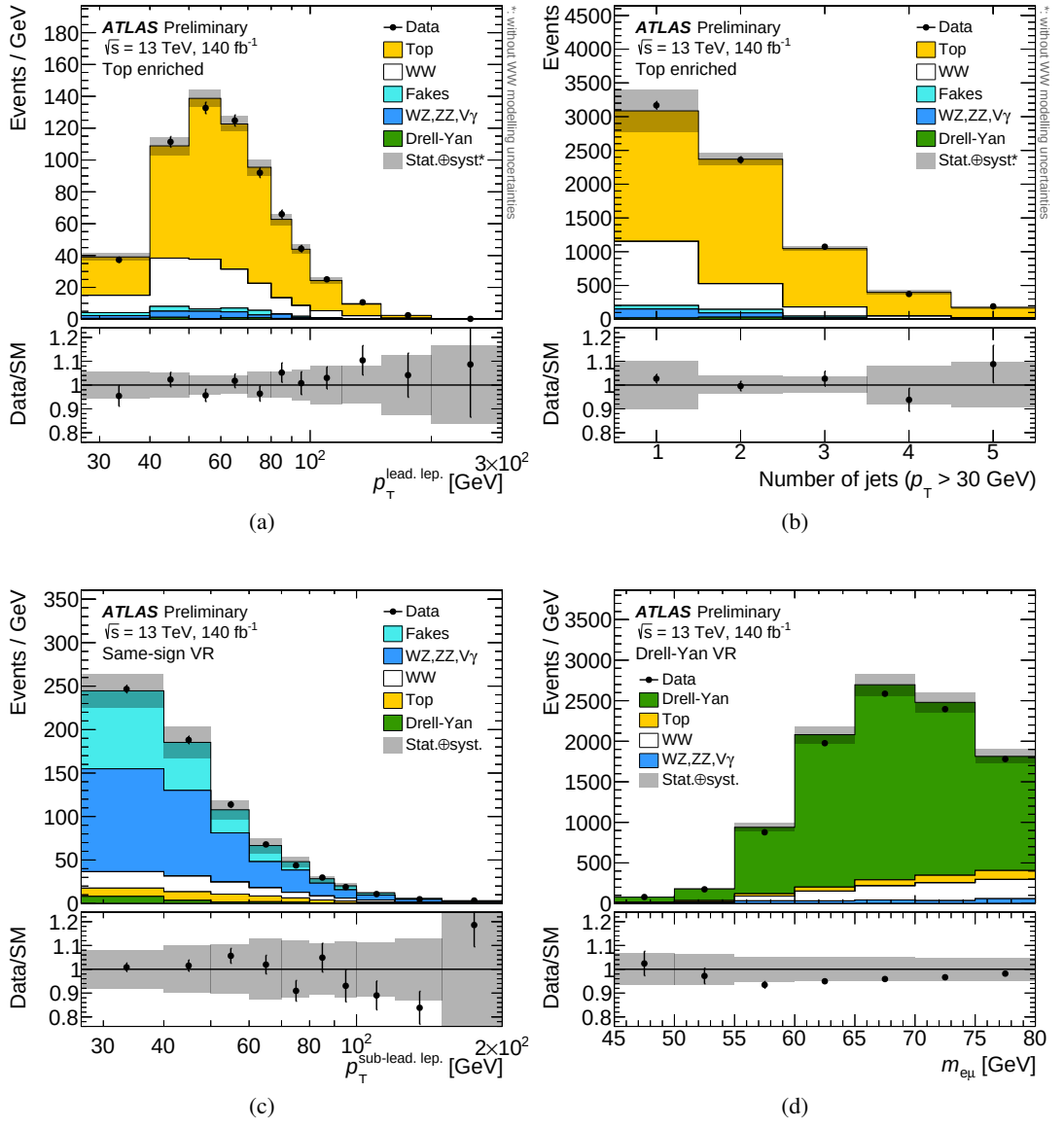

Figure 3: Detector-level distributions of (a) $p_{\mathrm{T}}^{\text{lead. lep.}}$ and (b) the jet multiplicity in the top-enriched region, (c) $p_{\mathrm{T}}^{\text{sub-lead. lep.}}$ in the same-sign validation region (VR), and (d) $m_{e\mu}$ in the Drell–Yan VR. The rightmost bin contains overflow events. Data are shown as black markers, together with histograms for the predictions of signal and background processes. The top-quark background in the top-enriched region is estimated using the data-driven method explained in Section 5.1; in the other two regions its contribution is small and the nominal MC prediction is used instead. The lower panels show the ratio of the data to the total prediction. The uncertainty bands shown include statistical and systematic uncertainties. Theory uncertainties on the signal are negligible and not shown.

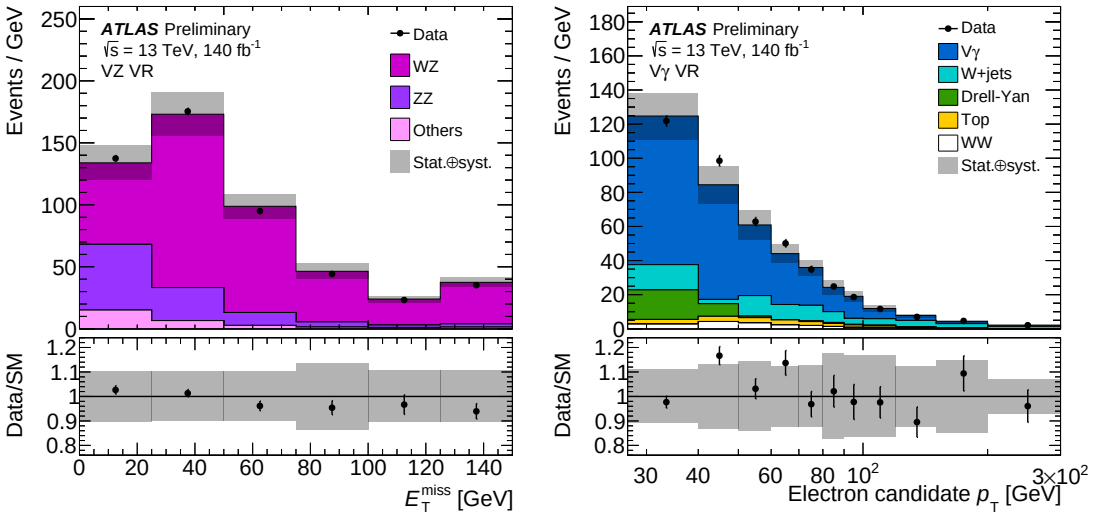

(a) (b)

Figure 4: Detector-level distributions of (a) $E_{\mathrm{T}}^{\mathrm{miss}}$ in the VZ VR and (b) the electron candidate p_{T} in the $V\gamma$ VR with opposite-charge leptons. The rightmost bin contains overflow events. Data are shown as black markers, together with histograms for the predictions of signal and background processes. The nominal MC prediction is used for the top-quark background in both regions. The lower panels show the ratio of the data to the total prediction. The uncertainty bands shown include statistical and systematic uncertainties. Theory uncertainties on the signal are negligible and not shown.

5.5 Selected WW candidate events

Table 3 lists the number of selected WW candidate events, as well as the breakdown of the background predictions. Details of the systematic uncertainties are given in Section 7. Figure 5 shows distributions at detector level and compares the observed data with the signal prediction and the background estimate. A small underprediction of the data at low invariant mass and low jet activity is observed. In these bins, WW production is expected to be the dominant contribution to the event yield.

6 Fiducial and differential cross-section determination

The WW cross-section is evaluated in the fiducial volume defined at particle level in Table 4. Exactly one electron and one muon of opposite electric charge, which do not originate from τ-lepton or hadron decays ("prompt" leptons) are required. The momenta of photons emitted in a cone of size $\Delta R = 0.1$ around the lepton direction that do not originate from hadron decays are added to the lepton momentum to form infrared-safe "dressed" leptons. Kinematic cuts on leptons reflect the analysis cuts and the invariant mass of the two leptons, $m_{e\mu}$, is required to be greater than 85 GeV. Events with additional prompt leptons fulfilling a looser p_{T} cut are vetoed. Stable final-state particles[5], excluding prompt neutrinos as well as prompt charged leptons and the associated photons, are clustered into particle-level jets using the anti-k_t algorithm with radius parameter $R = 0.4$. The nominal definition of the fiducial phase space includes a

[5] Particles are considered stable if their decay length $c\tau$ is greater than 1 cm.

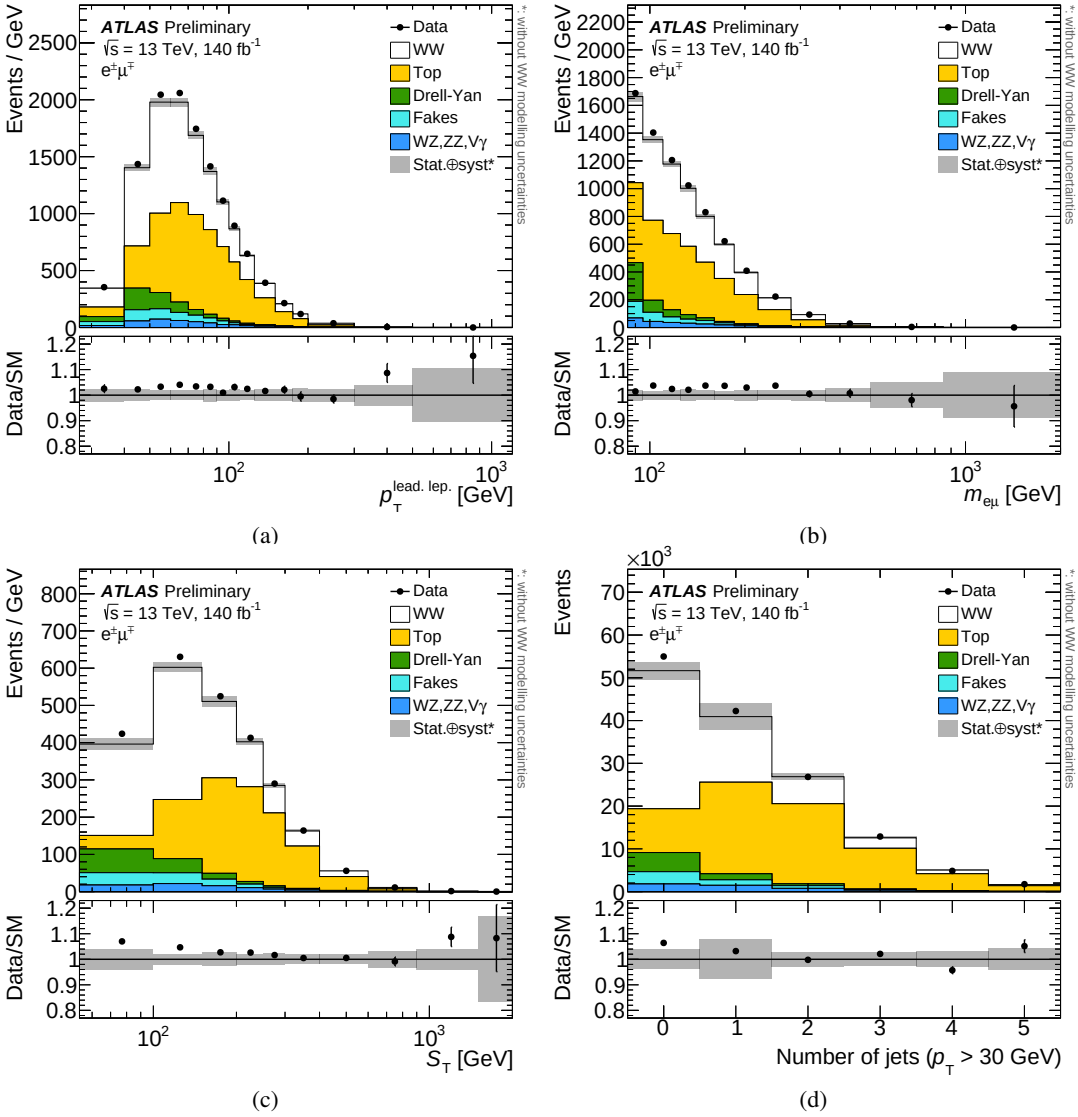

Figure 5: Detector-level distributions of (a) $p_{\mathrm{T}}^{\text{lead. lep.}}$, (b) $m_{e\mu}$, (c) S_{T}, and (d) the jet multiplicity. Data are shown as black markers together with histograms for the predictions of signal and background processes. The rightmost bin contains overflow events. The lower panels show the ratio of the data to the total prediction. Top and fake backgrounds are determined using data-driven methods. The uncertainty bands shown include statistical and systematic uncertainties, excluding theory uncertainties on the signal, which largely cancel in the measurement of WW cross-sections.

Table 4: Definition of the truth level objects and the fiducial phase space, with $\ell = e, \mu$ referring to prompt leptons and q_ℓ referring to the lepton electric charge. Jets containing b-hadrons are labeled "b-jet" while other jets are labeled "jet".

Object definition		
p_{T}^{ℓ}	$>$	27 GeV
$\lvert\eta^{\ell}\rvert$	$<$	2.5
$p_{\mathrm{T}}^{\ell,\,\mathrm{loose}}$	$>$	10 GeV
$\lvert\eta^{\ell,\,\mathrm{loose}}\rvert$	$<$	2.5
$p_{\mathrm{T}}^{b-\mathrm{jet}}$	$>$	20 GeV
$\lvert y^{b-\mathrm{jet}}\rvert$	$<$	2.5
$p_{\mathrm{T}}^{\mathrm{jet}}$	$>$	30 GeV
$\lvert y^{\mathrm{jet}}\rvert$	$<$	4.5

Fiducial selection requirements		
N_e	$=$	1
N_μ	$=$	1
$N_{\ell,\,\mathrm{loose}}$	$=$	2
$q_\mu \times q_e$	$=$	-1
$m_{e\mu}$	$>$	85 GeV
$N_{\text{b-jet}}$	$=$	0

veto on particle-level b-jets with $p_{\mathrm{T}} > 20$ GeV that are defined by ghost-association [90] of b-hadrons. The missing transverse momentum is defined at particle level as the negative vectorial sum of the transverse momenta of visible particles.

The integrated fiducial cross-section is determined using a profile likelihood fit of the S_{T} distribution. A model based on the sum of background estimates, which are determined using the data-driven methods in the case of top-pair production and fake-lepton events presented in Sections 5.1 and 5.2, is fit to the data, alongside the signal prediction which includes $q\bar{q} \to WW$ and $gg \to WW$ production as well as electroweak $WWjj$ production. The number of events in each bin is modelled as the predicted number of signal events scaled by a signal-strength modifier μ, plus the number of background events. The prediction of signal and background events is subject to uncertainties, which are parametrized by nuisance parameters. The likelihood is modelled using RooFit [91] as a product of Poissonian distributions multiplied by Gaussian constraints of nuisance parameters. The fiducial cross-section is obtained by multiplying the unconditional maximum-likelihood estimate of μ with the particle level fiducial cross-section prediction of the signal model. The fit of the S_{T} distribution reduces uncertainties associated with the top-quark background, which dominates at high S_{T} and, to a lesser extent, of Drell–Yan and fake-lepton uncertainties, which are most important at low S_{T}. As the fit relies on the correct prediction of the signal shape from MC simulation it is subject to signal modelling uncertainties and only valid for a SM-like WW signal.

The differential cross-sections are determined using an iterative Bayesian unfolding method [92, 93]. In contrast to the integrated cross-section measurement, these results only weakly depend on the signal model, which is only used to estimate detector resolution and efficiency, and remain approximately valid also in the presence of physics beyond the SM. Background events are subtracted based on the estimates discussed in Section 5. A fiducial correction is applied that takes into account events that are reconstructed in the signal region, but originate from outside the fiducial region (about 13% of selected events, mostly events with leptons from τ decays). The unfolding procedure corrects for migrations between bins in the distributions during the reconstruction of the events. Finally, efficiency corrections take into account events inside the fiducial region that are not reconstructed in the signal region due to detector inefficiencies (about 44% of events). To reduce bias on the true distribution given by the chosen theory prediction, the method can be

applied with multiple iterations, at the cost of an increased statistical uncertainty. Due to the good modelling of the data by simulation and relatively small migration effects the method converges quickly and only two iterations are required for most observables, except for the jet multiplicity distribution, which is subject to larger modelling uncertainties and unfolded using three iterations. The bias from using the simulation distributions as a prior in the unfolding is estimated by reweighting the simulation with a smooth function such that it closely resembles the background-subtracted data. This reweighted detector-level prediction is unfolded using the nominal unfolding set-up. The unfolding procedure is able to very accurately recover the generator-level distribution, indicating a negligible bias in the unfolding procedure.

7 Uncertainties

Systematic uncertainties in the WW cross-section measurements arise from experimental sources, the background determination, the procedures used to correct for detector effects, and theoretical uncertainties in the signal modelling. Systematic uncertainties on the differential cross sections are evaluated by repeating the unfolding procedure with simulations based on varied assumptions on signal, background, and detector model. The resulting uncertainties are symmetrized and added in quadrature. In the likelihood that is used to determine the integrated fiducial cross section, the same uncertainty sources are instead modelled by nuisance parameters that are profiled in the fit.

The dominant experimental systematic uncertainties arise in the determination of the b-tagging efficiency and mis-tag rates [83], the correction of the jet energy scale and resolution [81], and the luminosity measurement [16]. Experimental uncertainties also encompass uncertainties in the calibration of lepton trigger [72, 73], reconstruction, identification and isolation efficiencies [75, 76], the calibration of the lepton momentum or energy scale and resolution [75, 94], and the modelling of pile-up. All experimental uncertainties are evaluated by varying the respective calibrations, and propagating their effects through the analysis, affecting both the background estimates and the unfolding of detector effects. Both the effect of the total rate and the effect on the shape of distributions are taken into account for all sources of systematic uncertainties.

The estimate of the top-quark background is affected by the statistical uncertainty of the number of events in the control region, and by uncertainties in the modelling of $t\bar{t}$ and single-top Wt events, such as the uncertainty in the matrix element calculation, the parton shower modelling, the QCD scale choices, the initial- and final-state radiation and the interference between $t\bar{t}$ and single-top Wt events [95]. These are evaluated by using the alternative simulations described in Section 3 and propagating the results through the top-quark background estimate.

Systematic uncertainties in the estimate of fake leptons are derived by changing the selection used to estimate the extrapolation weights, in order to change the composition of the sources of fake leptons. Additionally, the subtraction of the prompt-lepton sources in the control region is varied, and the statistical uncertainties of the weights are propagated. More details on the uncertainties affecting the fake-lepton estimate can be found in Section 5.

The uncertainty in additional backgrounds is estimated by varying each of their cross-sections within their respective uncertainties and by using scale variations to account for missing higher-order QCD corrections and the parton shower model. The impact of these uncertainties on the cross-section measurements is small compared to the uncertainties associated with the fake lepton and top-quark background.

Table 5: Impacts of uncertainties on the integrated fiducial cross-section measurement with the profile likelihood fit. They are evaluated by varying each nuisance parameter individually within its post-fit uncertainty and quadratically adding the impacts for each uncertainty group. "Top modelling" and "Signal modelling" are uncertainties in the theoretical modelling of the respective processes, "Fake lepton background" is the uncertainty in the fake-lepton estimate while "Other background" is the uncertainty due to minor prompt-lepton backgrounds, "Flavour tagging" is all uncertainties in flavour tagging efficiency and mis-tag rate, "Jet calibration" uncertainties encompass jet energy scale and resolution uncertainties, and "Luminosity" is the uncertainty in the luminosity measurement. All systematic uncertainties belonging to none of the above categories are included in "Other systematic uncertainties". Statistical uncertainties arise in both the signal region and control region used for the data-driven top and fake-lepton estimates and also from backgrounds that are estimated using MC simulations.

Uncertainty source	Effect
Total uncertainty	3.1%
Stat. uncertainty	1.1%
Top modelling	1.6%
Fake lepton background	1.5%
Flavour tagging	0.7%
Other background	0.9%
Signal modelling	1.0%
Jet calibration	0.6%
Luminosity	0.8%
Other systematic uncertainties	0.9%

The uncertainty due to missing higher-order QCD corrections in the signal simulation is evaluated by varying the renormalization and factorization scales up and down by factors of two, avoiding opposite variations. The scale variation is performed in both matrix element and parton shower. Additional uncertainties on the parton shower are evaluated by varying the parameters of the A14 tune within their uncertainties, with the largest uncertainty resulting from the variation VAR3c [46], affecting the modelling of initial state radiation. An uncertainty on the modelling of heavy flavour jets is introduced by varying the fraction of events containing at least one jet originating from a b-quark or a c-quark by 30%, which covers the difference between predictions from Pythia8.230 and Sherpa2.2.2.

Statistical uncertainties in the unfolded distributions are evaluated by creating pseudo data samples that are obtained by varying the data within their Poisson uncertainties in each bin and then propagating these varied samples through the unfolding. The statistical uncertainties of the background estimates, which include statistical uncertainties in MC predictions and due to the control regions used in estimating the top and fake-lepton backgrounds, are evaluated using the same method.

Table 5 gives a breakdown of the uncertainties in the fiducial cross-section measured in the profile likelihood fit. Figures 6(a) and 6(b) display the uncertainties as a function of the unfolded $m_{e\mu}$ and S_{T} distributions, respectively.

8 Theoretical Predictions

Fiducial differential cross-section measurements are compared to three types of predictions.

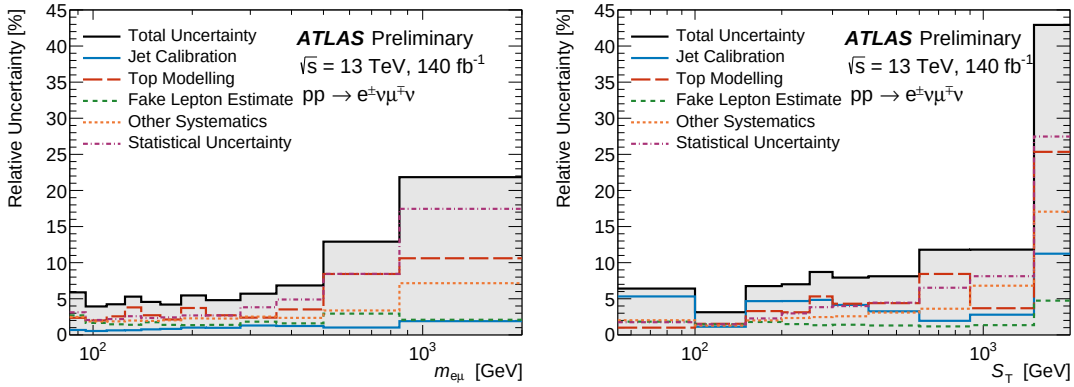

(a) (b)

Figure 6: Uncertainties on the unfolded (a) $m_{e\mu}$ and (b) S_{T} distributions. "Jet calibration" uncertainties encompass jet energy scale and resolution uncertainties, "Top modelling" are uncertainties in the theoretical modelling of the top-quark background, and "Fake Lepton Estimate" is the uncertainty in the estimate of the fake-lepton background. All systematic uncertainties related to minor prompt-lepton backgrounds, flavour tagging efficiencies and mis-tag rates, the luminosity, lepton calibration, pile-up reweighting, and signal modelling, are included in "Other systematics". "Statistical Uncertainty" combines statistical uncertainties that arise in both the signal region and control regions used for the data-driven top and fake-lepton estimates and also from backgrounds that are estimated using MC simulations.

The first is a fixed-order prediction calculated using MATRIX 2.0.1 [40, 41, 71, 96–105], which includes the NNLO QCD correction to $q\bar{q} \to WW$ production, and the NLO QCD correction to $gg \to WW$ production. The latter correction constitutes part of the N^{3}LO correction to WW production and the combined prediction is thus labeled nNNLO. The prediction also includes photon-induced contribution and NLO electroweak corrections using OpenLoops. The electroweak correction is combined, by default, multiplicatively with the QCD correction to $q\bar{q} \to WW$, with the exception of the photon-induced contributions, which is independently added to the cross-section prediction. In the tails of the $p_{\mathrm{T},e\mu}$, $E_{\mathrm{T}}^{\mathrm{miss}}$, and jet multiplicity distributions the multiplicative application of the NLO EW correction is not appropriate, as the correction primarily accounts for WW events with hard photon radiation. Hence the additive combination scheme is used for these observables. The NNPDF3.1nnlo [106] set of PDFs was used, with a prediction of the photon PDF with the luxQED method [107]. The factorization and renormalization scales were set to half the sum of W boson transverse masses [108]. Theoretical uncertainties due to missing higher-order QCD corrections are evaluated using 7-point variations of the factorization and renormalization scales by a factor of 2.

The second prediction is derived from the MiNNLO+Pythia8 $q\bar{q} \to WW$ sample in combination with the Sherpa 2.2.2 [32, 33] $gg \to WW$ sample. These samples are also used to estimate efficiencies as well as resolution, to model the WW signal in the maximum likelihood fit, and were already introduced in Section 3. The NNPDF3.0nnlo [30] set of PDFs was used in the generation of these samples while NNPDF3.1nnlo was used for the MATRIX prediction introduced above. Compared to the results from MATRIX, this prediction lacks photon-induced contributions as well as NLO electroweak corrections beyond the effects of photon radiation included in the Pythia parton shower and NLO corrections to the gluon-initiated sub-process. On the other hand, the inclusion of the parton shower effects improves the modelling of jets and distributions correlated to the transverse momentum of the WW system.

The third prediction was generated using Sherpa 2.2.12 [32]. The prediction is of NLO accuracy in QCD

Table 6: Comparison of theoretical predictions for fiducial cross-sections of various sub-processes contributing to WW production, with the corresponding scale uncertainties. The initial state label, for example in $q\bar{q} \to WW$, corresponds to the initial state at leading order. Other partons contribute to each sub-process at higher orders in perturbation theory. The names of the NNPDF3.0NNLO and NNPDF3.1NNLO LUXQED PDF sets are shortened in the table.

Process	Code	PDF	Perturbative order	Fid. cross-section	
$q\bar{q} \to WW$	MATRIX2.0.1	NNPDF3.1	NNLO QCD	674 fb	±1.8 %
$q\bar{q} \to WW$	MiNNLO + Pythia8	NNPDF3.0	NNLO QCD + PS	624 fb	±1.1 %
$q\bar{q} \to WW$	Sherpa2.2.12	NNPDF3.0	NLO QCD + PS †	630 fb	±7.2 %
$gg \to WW$	MATRIX2.0.1	NNPDF3.1	NLO QCD	32 fb	±13 %
$gg \to WW$	Sherpa2.2.2	NNPDF3.0	LO QCD + PS †	15 fb	±30 %
$\gamma\gamma \to WW$	MATRIX 2.0.1	NNPDF3.1	LO	5 fb	±2.3 %
$\gamma\gamma \to WW$	MATRIX 2.0.1	NNPDF3.1	NLO EW	11 fb	±2.3 %
$q\bar{q} \to WWjj$ (EW)	Sherpa2.2.12	NNPDF3.0	LO + PS	4 fb	±7.0 %
For calculation of NLO EW correction:					
$q\bar{q} \to WW$	MATRIX2.0.1	NNPDF3.1	LO	436 fb	±5.1 %
$q\bar{q} \to WW$	MATRIX2.0.1	NNPDF3.1	NLO EW	418 fb	±5.1 %

†: Includes matrix elements with additional parton emissions, matched and merged with the parton shower, which increases the accuracy of the simulation of high jet multiplicity events but also increases the nominal scale uncertainty.

for up to one additional parton, and leading-order accuracy for two to three additional parton emissions for $q\bar{q}$ initial states. The matrix element calculations were matched and merged with the Sherpa parton shower based on Catani–Seymour dipole factorization [34, 35] using the MEPS@NLO prescription [36–39]. The virtual QCD corrections were provided by the OpenLoops library [40, 41, 102]. The NNPDF3.0NNLO set of PDFs was used [30], along with the dedicated set of tuned parton-shower parameters developed by the Sherpa authors. This generator combination lacks the full NNLO QCD corrections but does include an extra parton emission at LO, which does improve the modelling of high-multiplicity events.

The last two predictions are augmented by a simulation of electroweak production of a diboson pair in association with two jets ($VVjj$), which was generated with the Sherpa 2.2.12 [32] generator. Inclusively the contribution of this sub-process is negligible but $WWjj$ production with vector boson scattering kinematics constitutes a correction of several percent in bins dominated by events with at least two jets.

A comparison of fiducial cross-section predictions is given in Table 6. The Powheg MiNNLO prediction for $q\bar{q} \to WW$, using NNPDF3.0NNLO, is 7% smaller than the fixed-order NNLO prediction using NNPDF3.1NNLO. The different PDF choice results in a 4% change in cross-section while parton shower effects, in particular final state photon radiation, reduce the lepton momenta and thus the signal acceptance by 3%. Sherpa2.2.12 predicts a fiducial cross-section that is similar to the one from Powheg MiNNLO, albeit with a larger scale uncertainty. The Sherpa2.2.2 $gg \to WW$ prediction at LO is significantly smaller than the MATRIX NLO QCD prediction. A k-factor of 1.7, calculated as the ratio of NLO and Sherpa cross-section in the total phase space is applied to the $gg \to WW$ sample and only partially compensates for the difference due to different predictions of the acceptance by both models. The NLO electroweak correction to $q\bar{q} \to WW$, given by the ratio of NLO EW to the LO prediction, decreases the $q\bar{q} \to WW$ cross-section by 4% while doubling the photon-induced contribution.

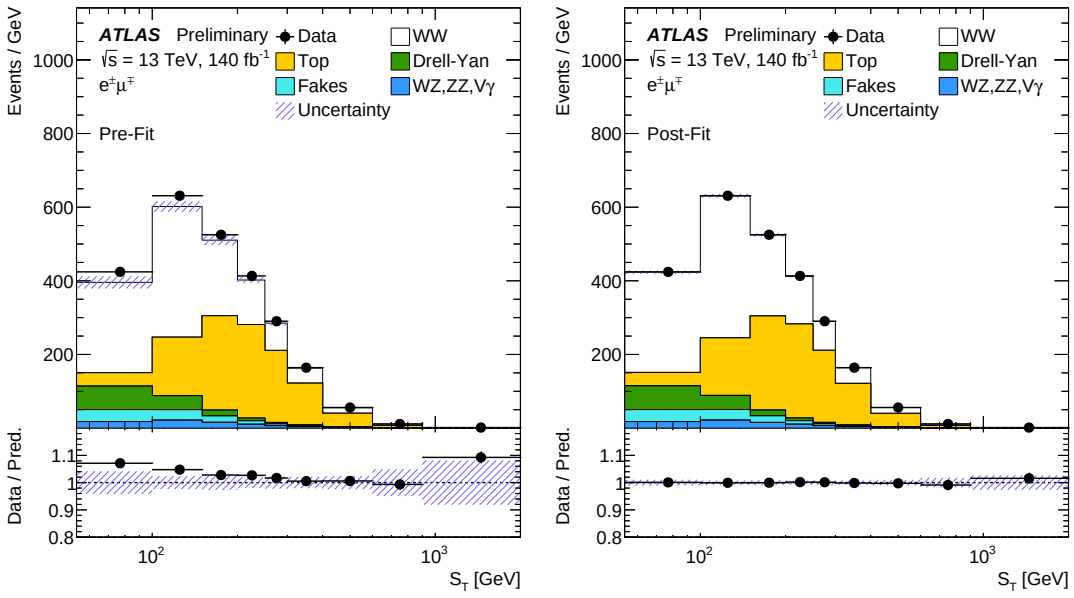

(a) (b)

Figure 7: (a) Pre-fit and (b) post-fit model for the profile likelihood fit in the S_{T} distribution. Data are shown as black markers together with the predictions for the signal and background production processes. The rightmost bin contains overflow events. The lower panels show the ratio of the data to the total prediction. Top and fake backgrounds are determined using data-driven methods. The uncertainty bands shown include statistical and systematic uncertainties. Theory uncertainties on the shape and efficiency of the signal are included.

9 Results

The measured fiducial cross-section for WW production, with $WW \to e^{\pm}\nu\mu^{\mp}\nu$, at $\sqrt{s} = 13\,\mathrm{TeV}$, for the fiducial volume defined in Table 4 is determined from the profile likelihood fit to be

$$\sigma_{\mathrm{fid}} = 707 \pm 7\ (\mathrm{stat.}) \pm 20\ (\mathrm{syst.})\ \mathrm{fb},$$

with a total uncertainty of 3.1%. Figures 7(a) and 7(b) present the pre-fit and post-fit distributions of S_{T}, respectively. In the fit, nuisance parameters remain very close to their initial values and the background normalizations are changed by less than 2% with respect to their estimates based on control regions and theoretical calculations. No individual nuisance parameter is constrained to more than 80% of its pre-fit uncertainty. However, uncertainties in post-fit yields and thus the uncertainty bands in Figure 7(b) are strongly reduced because nuisance parameter uncertainties are correlated post-fit such that variations that are incompatible with the observed yields are constrained.

In Figure 8 the result is compared to the nominal MiNNLO model used in the analysis, the Sherpa prediction introduced in Section 8, and the nNNLO QCD predictions of MATRIX 2.0.1 as well as the same nNNLO predictions combined with NLO electroweak corrections. While the measured cross-section is about two standard deviations larger than the cross-section predicted by MiNNLO, it agrees well with the MATRIX predictions. The main reasons for the larger cross-section predicted by MATRIX are the updated NNPDF PDF version, which increases the cross-section by 28 fb, and a 11 fb increase of the cross-section due to photon-induced contributions, as detailed in Section 8.

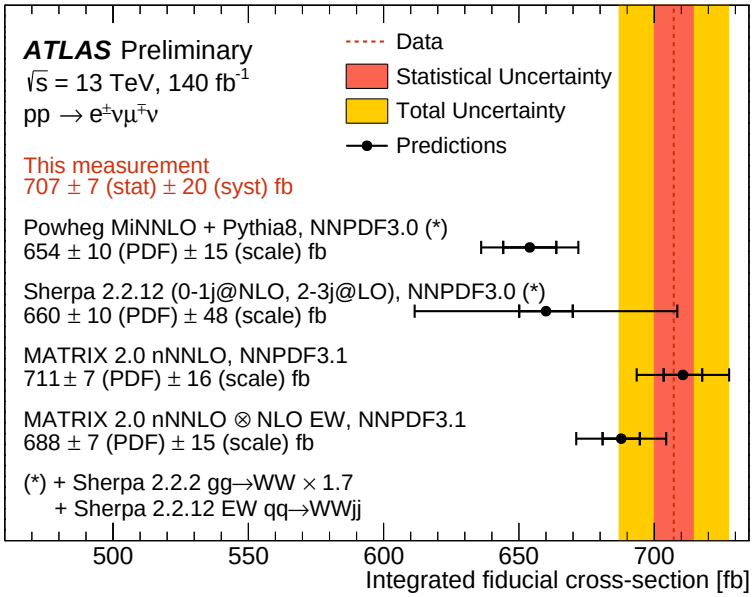

Figure 8: Measured fiducial cross-sections, compared to theoretical predictions from PowHeg MiNNLO, Sherpa2.2.12, and MATRIX 2.0.1. The nNNLO prediction includes photon-induced contributions and NLO QCD corrections to the gluon-induced initial state. The PowHeg MiNNLO and Sherpa2.2.12 predictions are combined with Sherpa2.2.2 and Sherpa2.2.12 to model gluon-induced WW production and the electroweak production of $WWjj$, respectively. An inclusive NLO k-factor of 1.7 is applied to the Sherpa2.2.2 prediction. Inner (outer) error bars on theory prediction correspond to PDF (the combination of scale and PDF) uncertainties.

The measurement is extrapolated to the full phase space of WW production based on the acceptance of 23.7% ± 0.3% for $W^+W^- \to e^\pm\nu\mu^\mp\nu$ events, calculated at nNNLO with MATRIX, including NLO electroweak corrections and by accounting for a leptonic W branching ratio of 10.86%. The uncertainty on the acceptance is 1.1%, estimated by varying the renormalization and factorization scales by factors of two, avoiding variations in opposite directions, by evaluating the PDF uncertainty, and by comparing the multiplicative with the additive scheme for electroweak corrections, with the last being the dominant uncertainty. After this extrapolation, the measured total production cross-section of W-boson pairs is found to be

$$\sigma_{\text{total}} = 127 \pm 1\ (\text{stat.}) \pm 4\ (\text{syst.})\ \text{pb}.$$

In Figure 9 the total cross-section is compared to measurements of ATLAS [10] and CMS [9] that are based on datasets of 36 fb^{-1}. The improved precision of this measurement with respect to its predecessor [8] is due to more precise data-driven top quark and fake lepton estimates, the improved luminosity determination [16], and the measurement in a jet-inclusive phase space, which reduces jet-related uncertainties as well as theoretical uncertainties on the extrapolation to the full phase space.

Differential fiducial cross-sections are presented in Figure 10 and 11. Excellent agreement with the fixed-order MATRIX prediction is observed. Electroweak corrections, applied with the multiplicative combination scheme, improve the modelling of high-mass events for some distributions (e.g. $m_{e\mu}$) but over-correct for other distributions (e.g. $p_{\text{T}}^{\text{lead. lep.}}$). The over-correction is expected as the multiplicative combination scheme does not always yield an appropriate estimate of mixed QCD-EW effects, in particular in regions of phase space that are dominated by events with hard QCD radiation, as is the case for high $p_{\text{T}}^{\text{lead. lep.}}$ [108]. The parton-shower matched predictions based on the MiNNLO and Sherpa 2.2.12 samples

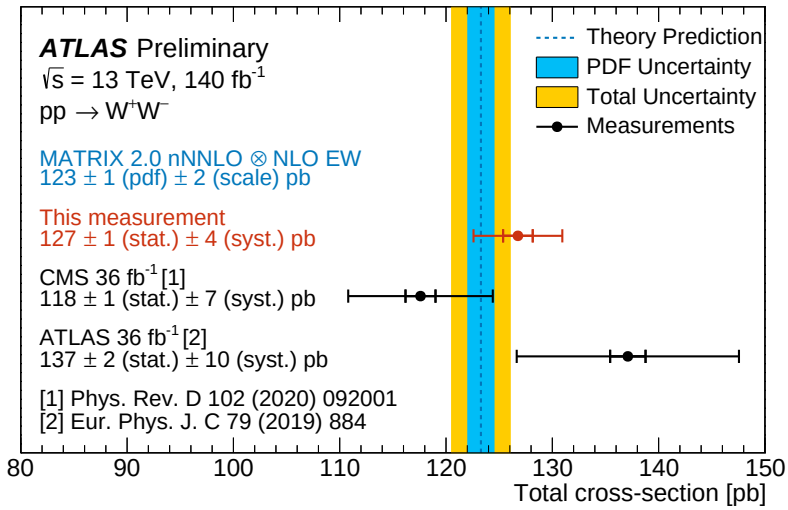

Figure 9: Measured total WW cross-sections, compared to a theoretical prediction from MATRIX+OpenLoops [108] and previous measurements of ATLAS [8] and CMS [9]. The theoretical prediction uses the NNPDF3.1nnlo luxQED set of parton distribution functions, is of NNLO accuracy in QCD for $q\bar{q} \to WW$ production and includes NLO QCD corrections to $gg \to WW$ production, which constitute part of the N^{3}LO correction. It includes photon-induced contributions and is combined multiplicatively with NLO EW corrections to $q\bar{q} \to WW$. Inner (outer) error bars on experimental measurements correspond to statistical (total) uncertainty. The inner (outer) error band includes PDF uncertainties (PDF and scale uncertainties added in quadrature).

model the data well except for an under-prediction of the cross-section most regions of phase space, which can largely be explained by the different PDF choice. The parton shower improves the modelling at low diboson transverse momentum, as can be seen in the $p_{\mathrm{T},e\mu}$ distribution, and allows for the simulation of events with more than two jets.

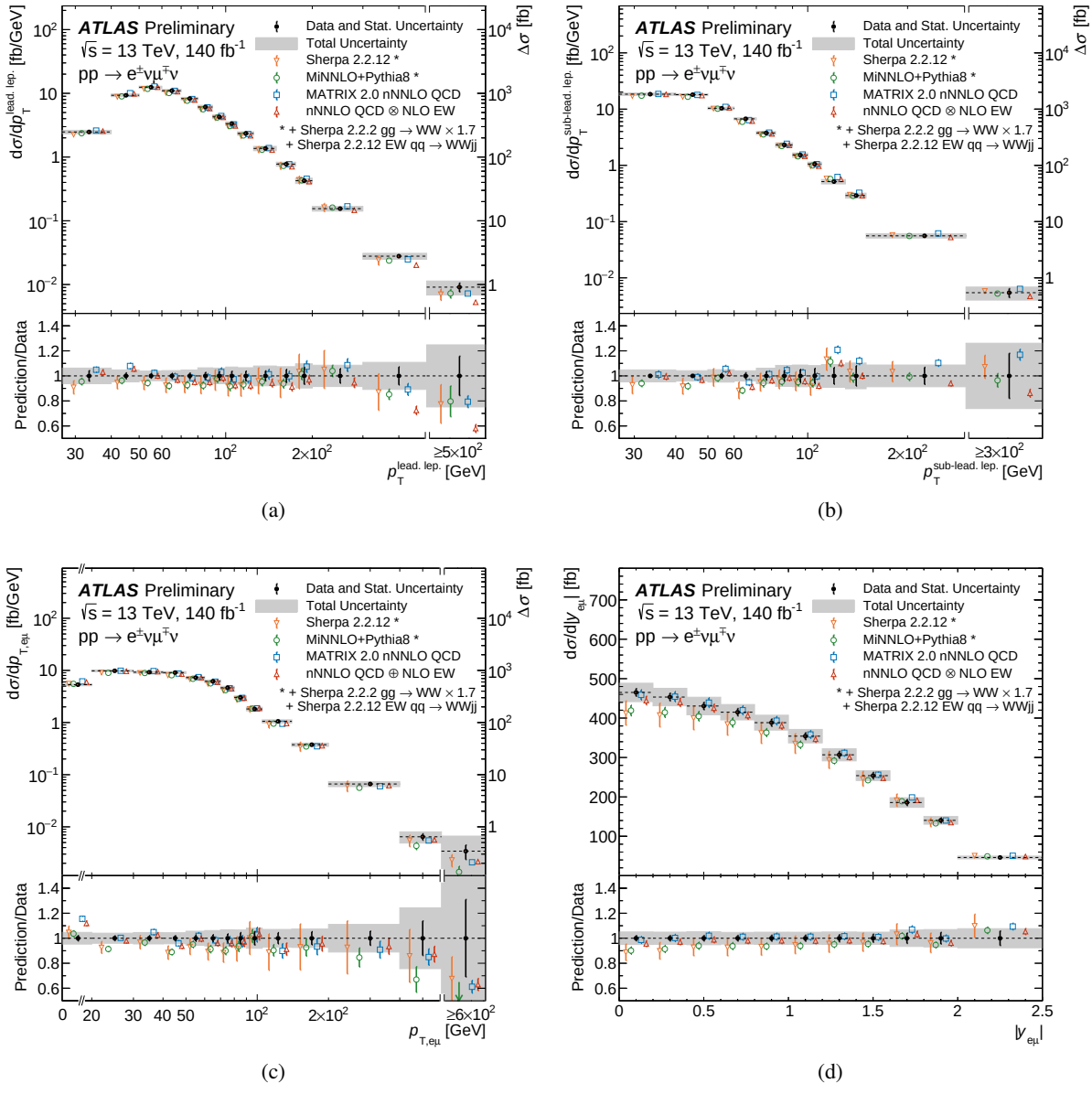

Figure 10: Fiducial differential cross-sections as a function of (a) $p_{\mathrm{T}}^{\text{lead. lep.}}$, (b) $p_{\mathrm{T}}^{\text{sub-lead. lep.}}$, (c) $p_{\mathrm{T},e\mu}$, and (d) $y_{e\mu}$. The measured cross-section values are shown as points with error bars giving the statistical uncertainty and solid bands indicating the size of the total uncertainty. For distributions in which the rightmost bin is inclusive, the right-hand-side axis indicates the integrated cross-section of the rightmost bin. The results are compared to fixed-order nNNLO QCD + NLO EW predictions of MATRIX 2.0.1, with the NNLO + PS predictions from POWHEG MiNNLO + PYTHIA8, and SHERPA2.2.12 NLO + PS predictions. The last two predictions are combined with SHERPA2.2.2 for the gg initial state and SHERPA2.2.12 for electroweak $WWjj$ production. These contributions are modelled at LO but a NLO QCD k-factor of 1.7 is applied for gluon induced production. Theoretical predictions are indicated as markers with vertical lines denoting PDF, scale and parton shower uncertainties. Markers are staggered for better visibility.

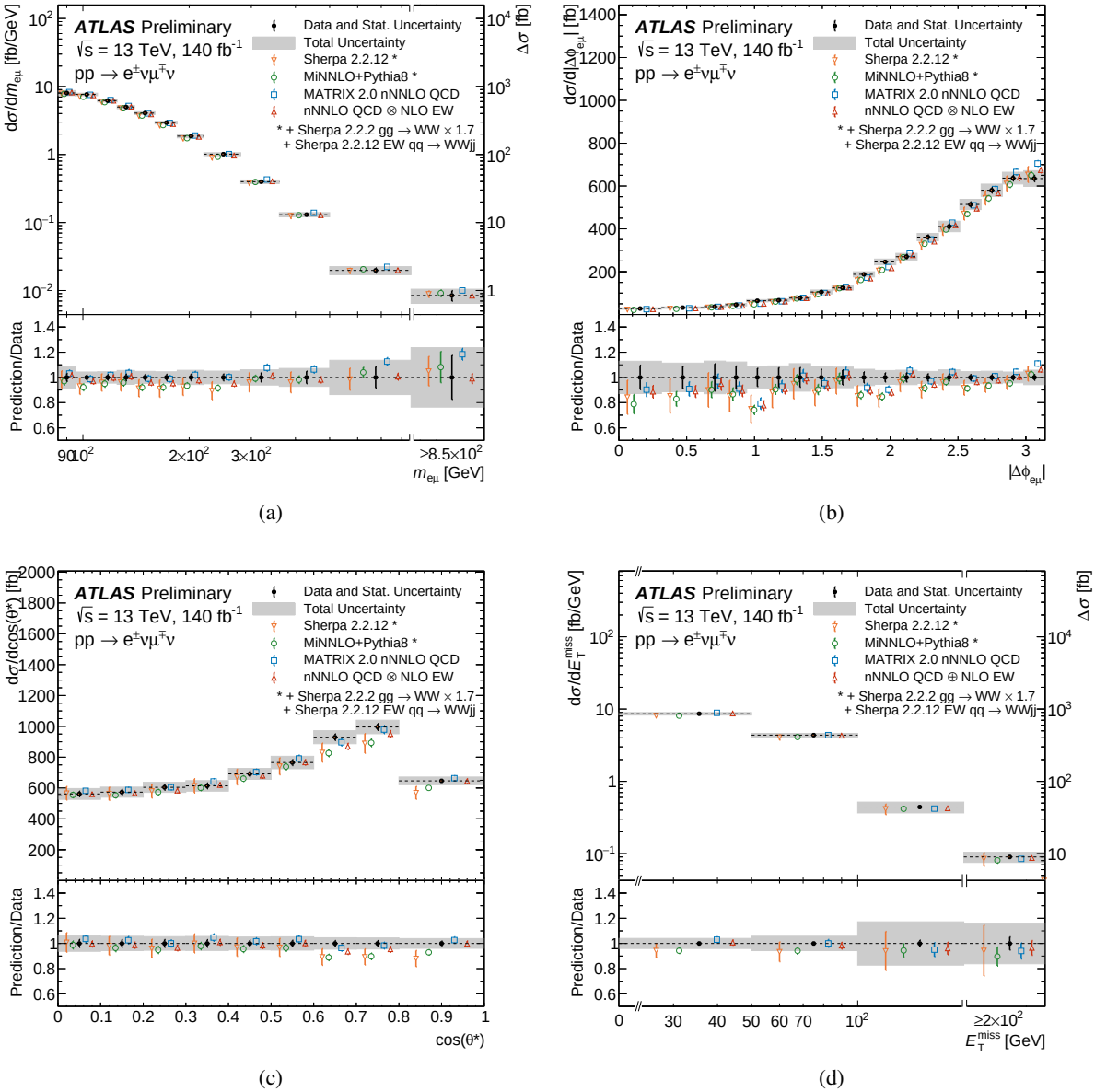

Figure 11: Fiducial differential cross-sections as a function of (a) $m_{e\mu}$, (b) $|\Delta\phi_{e\mu}|$, (c) $\cos\theta^*$, and (d) $E_{\mathrm{T}}^{\mathrm{miss}}$. The measured cross-section values are shown as points with error bars giving the statistical uncertainty and solid bands indicating the size of the total uncertainty. For distributions in which the rightmost bin is inclusive, the right-hand-side axis indicates the integrated cross-section of the rightmost bin. The results are compared to fixed-order nNNLO QCD + NLO EW predictions of MATRIX 2.0.1, with the NNLO + PS predictions from POWHEG MiNNLO + PYTHIA8, and SHERPA2.2.12 NLO + PS predictions. The last two predictions are combined with SHERPA2.2.2 for the gg initial state and SHERPA2.2.12 for electroweak $WWjj$ production. These contributions are modelled at LO but a NLO QCD k-factor of 1.7 is applied for gluon induced production. Theoretical predictions are indicated as markers with vertical lines denoting PDF, scale and parton shower uncertainties. Markers are staggered for better visibility.

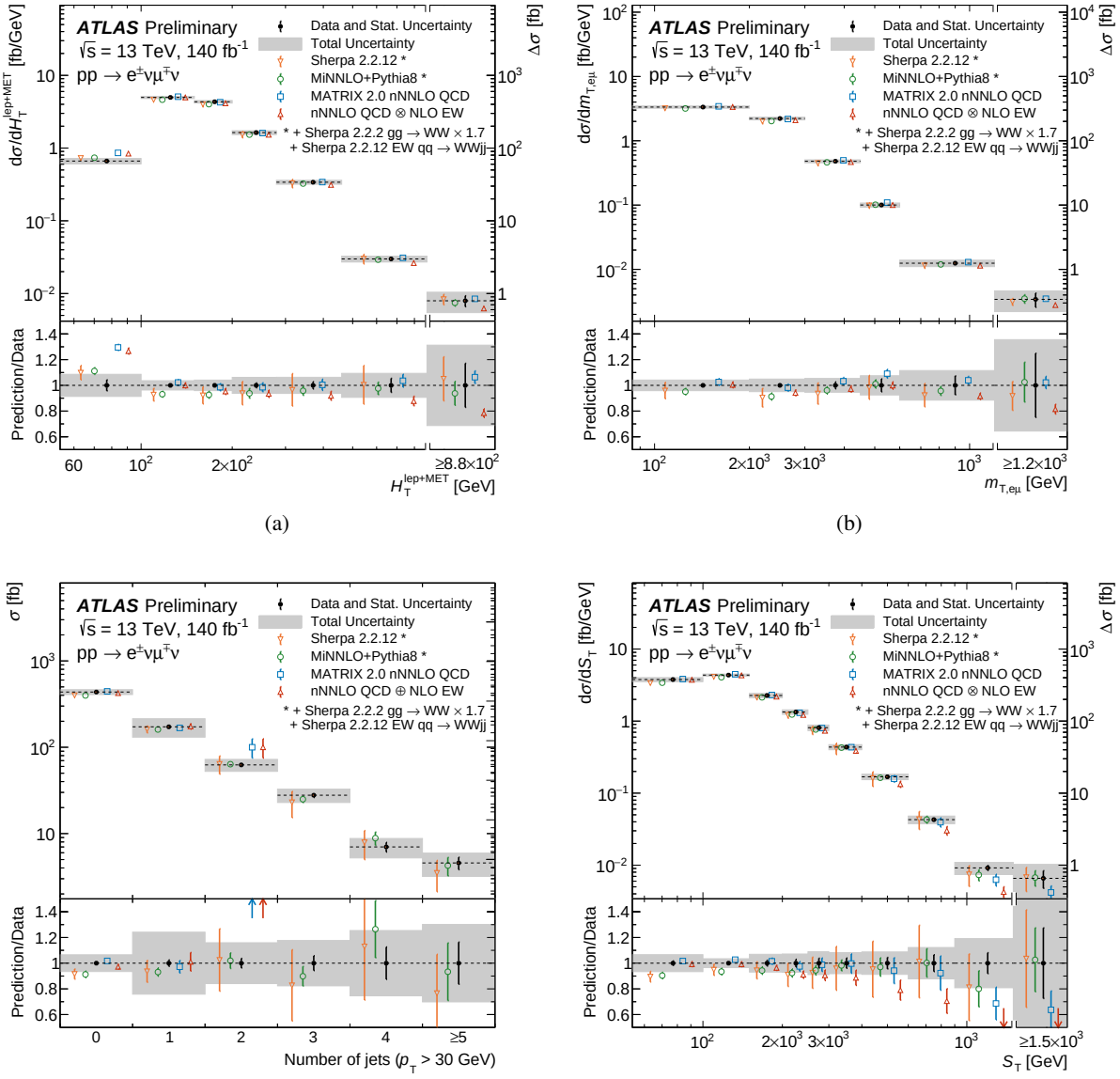

Figure 12: Fiducial differential cross-sections as a function of (a) $H_{\mathrm{T}}^{\mathrm{lep.+MET}}$, (b) $m_{\mathrm{T},e\mu}$, (c) the jet multiplicity of the event, and (d) S_{T}. The measured cross-section values are shown as points with error bars giving the statistical uncertainty and solid bands indicating the size of the total uncertainty. For distributions in which the rightmost bin is inclusive, the right-hand-side axis indicates the integrated cross-section of the rightmost bin. The results are compared to fixed-order nNNLO QCD + NLO EW predictions of MATRIX 2.0.1, with the NNLO + PS predictions from POWHEG MINNLO + PYTHIA8, and SHERPA2.2.12 NLO + PS predictions. The last two predictions are combined with SHERPA2.2.2 for the gg initial state and SHERPA2.2.12 for electroweak $WWjj$ production. These contributions are modelled at LO but a NLO QCD k-factor of 1.7 is applied for gluon induced production. Theoretical predictions are indicated as markers with vertical lines denoting PDF, scale and parton shower uncertainties. Markers are staggered for better visibility.

10 Conclusion

The measurement of W-boson pairs at hadron colliders is an important test of the Standard Model. It is sensitive to the self-couplings of vector bosons and provides a test of the electroweak theory as well as perturbative quantum chromodynamics.

A dataset corresponding to an integrated luminosity of $140\,\text{fb}^{-1}$, recorded between 2015 and 2018 by the ATLAS detector at the Large Hadron Collider in pp collisions at $\sqrt{s} = 13\,\text{TeV}$ is analyzed. Fiducial differential and integrated cross sections of W-boson pairs decaying into one electron and one muon of opposite electric charge are measured. A jet-inclusive event selection allows for the comparison to precise theoretical cross-section calculations while an improved data-driven estimates of the top-quark and fake lepton background reduce the uncertainty in the fiducial cross-section to 3.1% The measurement is extrapolated to the full phase space, resulting in a total WW cross-section of 127 ± 4 pb. Differential cross-sections are measured as a function of twelve observables.

The measurements are compared to state-of-the art theoretical predictions. A fixed-order prediction at nNNLO QCD [97] using NNPDF3.1NNLO LUXQED [106, 107] is in excellent agreement with the measured total cross-section and a gives a good description of differential cross-sections. The multiplicative combination with EW corrections improves the description of some observables while it does not represent an adequate description in other cases, as the combination cannot take into account non-factorizing EW-QCD effects [108]. Parton-shower matched predictions generated with POWHEG MINNLO [28] + PYTHIA8 [31] and SHERPA 2.2.12 [32] better describe bins dominated by events small WW p_{T} or high jet activity. Considering experimental and theoretical uncertainties, excellent agreement of the measurements with predictions is observed.

References

[1] CMS Collaboration, *Measurements of the electroweak diboson production cross sections in proton-proton collisions at $\sqrt{s} = 5.02$ TeV using leptonic decays*, Phys. Rev. Lett. **127** (2021) 191801, arXiv: 2107.01137 [hep-ex] (cit. on p. 2).

[2] ATLAS Collaboration, *Measurement of W^+W^- production in pp collisions at $\sqrt{s} = 7$ TeV with the ATLAS detector and limits on anomalous WWZ and $WW\gamma$ couplings*, Phys. Rev. D **87** (2013) 112001, arXiv: 1210.2979 [hep-ex] (cit. on p. 2), Erratum: Phys. Rev. D **88** (2013) 079906.

[3] CMS Collaboration, *Measurement of the W^+W^- cross section in pp collisions at $\sqrt{s} = 7$ TeV and limits on anomalous $WW\gamma$ and WWZ couplings*, Eur. Phys. J. C **73** (2013) 2610, arXiv: 1306.1126 [hep-ex] (cit. on p. 2).

[4] ATLAS Collaboration, *Measurement of total and differential W^+W^- production cross sections in proton–proton collisions at $\sqrt{s} = 8$ TeV with the ATLAS detector and limits on anomalous triple-gauge-boson couplings*, JHEP **09** (2016) 029, arXiv: 1603.01702 [hep-ex] (cit. on p. 2).

[5] CMS Collaboration, *Measurement of the W^+W^- cross section in pp collisions at $\sqrt{s} = 8$ TeV and limits on anomalous gauge couplings*, Eur. Phys. J. C **76** (2016) 401, arXiv: 1507.03268 [hep-ex] (cit. on p. 2).

[6] ATLAS Collaboration, *Measurement of W^+W^- production in association with one jet in proton–proton collisions at $\sqrt{s}$ = 8 TeV with the ATLAS detector*, Phys. Lett. B **763** (2016) 114, arXiv: 1608.03086 [hep-ex] (cit. on p. 2).

[7] ATLAS Collaboration, *Measurement of the W^+W^- production cross section in pp collisions at a centre-of-mass energy of $\sqrt{s}$ = 13 TeV with the ATLAS experiment*, Phys. Lett. B **773** (2017) 354, arXiv: 1702.04519 [hep-ex] (cit. on p. 2).

[8] ATLAS Collaboration, *Measurement of fiducial and differential W^+W^- production cross-sections at $\sqrt{s}$ = 13 TeV with the ATLAS detector*, Eur. Phys. J. C **79** (2019) 884, arXiv: 1905.04242 [hep-ex] (cit. on pp. 2, 22, 23).

[9] CMS Collaboration, *W^+W^- boson pair production in proton–proton collisions at $\sqrt{s}$ = 13 TeV*, Phys. Rev. D **102** (2020) 092001, arXiv: 2009.00119 [hep-ex] (cit. on pp. 2, 22, 23).

[10] ATLAS Collaboration, *Measurements of W^+W^- + ≥ 1 jet production cross-sections in pp collisions at $\sqrt{s}$ = 13 TeV with the ATLAS detector*, JHEP **06** (2021) 003, arXiv: 2103.10319 [hep-ex] (cit. on pp. 2, 8, 22).

[11] ATLAS Collaboration, *Measurements of W^+W^- production in decay topologies inspired by searches for electroweak supersymmetry*, (2022), arXiv: 2206.15231 [hep-ex] (cit. on p. 2).

[12] ALEPH, DELPHI, L3 and OPAL Collaborations and the LEP Electroweak Working Group, *Electroweak measurements in electron–positron collisions at W-boson-pair energies at LEP*, Phys. Rept. **532** (2013) 119, arXiv: 1302.3415 [hep-ex] (cit. on p. 2).

[13] CDF Collaboration, *Observation of W^+W^- production in $\bar{p}p$ collisions at $\sqrt{s}$ = 1.8 TeV*, Phys. Rev. Lett. **78** (1997) 4536 (cit. on p. 2).

[14] CDF Collaboration, *Measurement of the W^+W^- Production Cross Section and Search for Anomalous $WW\gamma$ and WWZ Couplings in $p\bar{p}$ Collisions at $\sqrt{s}$ = 1.96 TeV*, Phys. Rev. Lett. **104** (2010) 201801, [Erratum: Phys. Rev. Lett. 105 (2010) 019905], arXiv: 0912.4500 [hep-ex] (cit. on p. 2).

[15] DØ Collaboration, *Measurement of the WW Production Cross Section with Dilepton Final States in $p\bar{p}$ Collisions at $\sqrt{s}$ = 1.96 TeV and Limits on Anomalous Trilinear Gauge Couplings*, Phys. Rev. Lett. **103** (2009) 191801, arXiv: 0904.0673 [hep-ex] (cit. on p. 2).

[16] ATLAS Collaboration, *Luminosity determination in pp collisions at $\sqrt{s}$ = 13 TeV using the ATLAS detector at the LHC*, (2022), arXiv: 2212.09379 [hep-ex] (cit. on pp. 2, 4, 17, 22).

[17] P. Meade, H. Ramani and M. Zeng, *Transverse momentum resummation effects in W^+W^- measurements*, Phys. Rev. D **90** (2014) 114006, arXiv: 1407.4481 [hep-ph] (cit. on p. 2).

[18] A. Barr, *Measuring slepton spin at the LHC*, JHEP **02** (2006) 042, arXiv: hep-ph/0511115 (cit. on p. 3).

[19] ATLAS Collaboration, *The ATLAS Experiment at the CERN Large Hadron Collider*, JINST **3** (2008) S08003 (cit. on p. 4).

[20] L. Evans and P. Bryant, *LHC Machine*, JINST **3** (2008) S08001 (cit. on p. 4).

[21] ATLAS Collaboration, *ATLAS Insertable B-Layer Technical Design Report*, ATLAS-TDR-19; CERN-LHCC-2010-013, 2010, URL: https://cds.cern.ch/record/1291633 (cit. on p. 4), Addendum: ATLAS-TDR-19-ADD-1; CERN-LHCC-2012-009, 2012, URL: https://cds.cern.ch/record/1451888.

[22] B. Abbott et al., *Production and integration of the ATLAS Insertable B-Layer*, JINST **13** (2018) T05008, arXiv: 1803.00844 [physics.ins-det] (cit. on p. 4).

[23] ATLAS Collaboration, *The ATLAS Collaboration Software and Firmware*, ATL-SOFT-PUB-2021-001, 2021, URL: https://cds.cern.ch/record/2767187 (cit. on p. 4).

[24] ATLAS Collaboration, *ATLAS data quality operations and performance for 2015–2018 data-taking*, JINST **15** (2020) P04003, arXiv: 1911.04632 [physics.ins-det] (cit. on p. 4).

[25] G. Avoni et al., *The new LUCID-2 detector for luminosity measurement and monitoring in ATLAS*, JINST **13** (2018) P07017 (cit. on p. 4).

[26] ATLAS Collaboration, *The ATLAS Simulation Infrastructure*, Eur. Phys. J. C **70** (2010) 823, arXiv: 1005.4568 [physics.ins-det] (cit. on p. 4).

[27] GEANT4 Collaboration, S. Agostinelli et al., *GEANT4 – a simulation toolkit*, Nucl. Instrum. Meth. A **506** (2003) 250 (cit. on p. 4).

[28] D. Lombardi, M. Wiesemann and G. Zanderighi, *W^+W^- production at NNLO+PS with MINNLO$_{PS}$*, JHEP **11** (2021) 230, arXiv: 2103.12077 [hep-ph] (cit. on pp. 4, 27).

[29] P. F. Monni, P. Nason, E. Re, M. Wiesemann and G. Zanderighi, *MiNNLO$_{PS}$: a new method to match NNLO QCD to parton showers*, JHEP **05** (2020) 143, [Erratum: JHEP 02, 031 (2022)], arXiv: 1908.06987 [hep-ph] (cit. on p. 4).

[30] R. D. Ball et al., *Parton distributions for the LHC run II*, JHEP **04** (2015) 040, arXiv: 1410.8849 [hep-ph] (cit. on pp. 4, 5, 19, 20).

[31] T. Sjöstrand et al., *An introduction to PYTHIA 8.2*, Comput. Phys. Commun. **191** (2015) 159, arXiv: 1410.3012 [hep-ph] (cit. on pp. 4, 5, 27).

[32] E. Bothmann et al., *Event generation with Sherpa 2.2*, SciPost Phys. **7** (2019) 034, arXiv: 1905.09127 [hep-ph] (cit. on pp. 5, 19, 20, 27).

[33] F. Cascioli et al., *Precise Higgs-background predictions: merging NLO QCD and squared quark-loop corrections to four-lepton + 0,1 jet production*, JHEP **01** (2014) 046, arXiv: 1309.0500 [hep-ph] (cit. on pp. 5, 19).

[34] T. Gleisberg and S. Höche, *Comix, a new matrix element generator*, JHEP **12** (2008) 039, arXiv: 0808.3674 [hep-ph] (cit. on pp. 5, 6, 20).

[35] S. Schumann and F. Krauss, *A parton shower algorithm based on Catani–Seymour dipole factorisation*, JHEP **03** (2008) 038, arXiv: 0709.1027 [hep-ph] (cit. on pp. 5, 6, 20).

[36] S. Höche, F. Krauss, M. Schönherr and F. Siegert, *A critical appraisal of NLO+PS matching methods*, JHEP **09** (2012) 049, arXiv: 1111.1220 [hep-ph] (cit. on pp. 5, 6, 20).

[37] S. Höche, F. Krauss, M. Schönherr and F. Siegert,
QCD matrix elements + parton showers. The NLO case, JHEP **04** (2013) 027,
arXiv: 1207.5030 [hep-ph] (cit. on pp. 5, 6, 20).

[38] S. Catani, F. Krauss, B. R. Webber and R. Kuhn, *QCD Matrix Elements + Parton Showers*,
JHEP **11** (2001) 063, arXiv: hep-ph/0109231 (cit. on pp. 5, 6, 20).

[39] S. Höche, F. Krauss, S. Schumann and F. Siegert, *QCD matrix elements and truncated showers*,
JHEP **05** (2009) 053, arXiv: 0903.1219 [hep-ph] (cit. on pp. 5, 6, 20).

[40] F. Cascioli, P. Maierhöfer and S. Pozzorini, *Scattering Amplitudes with Open Loops*,
Phys. Rev. Lett. **108** (2012) 111601, arXiv: 1111.5206 [hep-ph] (cit. on pp. 5, 19, 20).

[41] A. Denner, S. Dittmaier and L. Hofer,
Collier: A fortran-based complex one-loop library in extended regularizations,
Comput. Phys. Commun. **212** (2017) 220, arXiv: 1604.06792 [hep-ph] (cit. on pp. 5, 19, 20).

[42] S. Frixione, G. Ridolfi and P. Nason,
A positive-weight next-to-leading-order Monte Carlo for heavy flavour hadroproduction,
JHEP **09** (2007) 126, arXiv: 0707.3088 [hep-ph] (cit. on p. 5).

[43] P. Nason, *A new method for combining NLO QCD with shower Monte Carlo algorithms*,
JHEP **11** (2004) 040, arXiv: hep-ph/0409146 (cit. on p. 5).

[44] S. Frixione, P. Nason and C. Oleari,
Matching NLO QCD computations with parton shower simulations: the POWHEG method,
JHEP **11** (2007) 070, arXiv: 0709.2092 [hep-ph] (cit. on p. 5).

[45] S. Alioli, P. Nason, C. Oleari and E. Re, *A general framework for implementing NLO calculations in shower Monte Carlo programs: the POWHEG BOX*, JHEP **06** (2010) 043,
arXiv: 1002.2581 [hep-ph] (cit. on p. 5).

[46] ATLAS Collaboration, *ATLAS Pythia 8 tunes to 7 TeV data*, ATL-PHYS-PUB-2014-021, 2014,
URL: https://cds.cern.ch/record/1966419 (cit. on pp. 4, 5, 18).

[47] R. D. Ball et al., *Parton distributions with LHC data*, Nucl. Phys. B **867** (2013) 244,
arXiv: 1207.1303 [hep-ph] (cit. on p. 5).

[48] ATLAS Collaboration, *Studies on top-quark Monte Carlo modelling for Top2016*,
ATL-PHYS-PUB-2016-020, 2016, URL: https://cds.cern.ch/record/2216168
(cit. on p. 5).

[49] S. Frixione, E. Laenen, P. Motylinski, C. White and B. R. Webber,
Single-top hadroproduction in association with a W boson, JHEP **07** (2008) 029,
arXiv: 0805.3067 [hep-ph] (cit. on p. 5).

[50] ATLAS Collaboration,
Studies on top-quark Monte Carlo modelling with Sherpa and MG5_aMC@NLO,
ATL-PHYS-PUB-2017-007, 2017, URL: https://cds.cern.ch/record/2261938
(cit. on p. 5).

[51] M. Bähr et al., *Herwig++ physics and manual*, Eur. Phys. J. C **58** (2008) 639,
arXiv: 0803.0883 [hep-ph] (cit. on p. 5).

[52] J. Bellm et al., *Herwig 7.0/Herwig++ 3.0 release note*, Eur. Phys. J. C **76** (2016) 196,
arXiv: 1512.01178 [hep-ph] (cit. on p. 5).

[53] L. A. Harland-Lang, A. D. Martin, P. Motylinski and R. S. Thorne,
Parton distributions in the LHC era: MMHT 2014 PDFs, Eur. Phys. J. C **75** (2015) 204,
arXiv: 1412.3989 [hep-ph] (cit. on p. 5).

[54] J. Alwall et al., *The automated computation of tree-level and next-to-leading order differential cross sections, and their matching to parton shower simulations*, JHEP **07** (2014) 079,
arXiv: 1405.0301 [hep-ph] (cit. on p. 5).

[55] M. Beneke, P. Falgari, S. Klein and C. Schwinn,
Hadronic top-quark pair production with NNLL threshold resummation,
Nucl. Phys. B **855** (2012) 695, arXiv: 1109.1536 [hep-ph] (cit. on p. 6).

[56] M. Cacciari, M. Czakon, M. Mangano, A. Mitov and P. Nason, *Top-pair production at hadron colliders with next-to-next-to-leading logarithmic soft-gluon resummation*,
Phys. Lett. B **710** (2012) 612, arXiv: 1111.5869 [hep-ph] (cit. on p. 6).

[57] P. Bärnreuther, M. Czakon and A. Mitov, *Percent-Level-Precision Physics at the Tevatron: Next-to-Next-to-Leading Order QCD Corrections to $q\bar{q} \to t\bar{t} + X$*,
Phys. Rev. Lett. **109** (2012) 132001, arXiv: 1204.5201 [hep-ph] (cit. on p. 6).

[58] M. Czakon and A. Mitov,
NNLO corrections to top-pair production at hadron colliders: the all-fermionic scattering channels,
JHEP **12** (2012) 054, arXiv: 1207.0236 [hep-ph] (cit. on p. 6).

[59] M. Czakon and A. Mitov,
NNLO corrections to top pair production at hadron colliders: the quark-gluon reaction,
JHEP **01** (2013) 080, arXiv: 1210.6832 [hep-ph] (cit. on p. 6).

[60] M. Czakon, P. Fiedler and A. Mitov,
Total Top-Quark Pair-Production Cross Section at Hadron Colliders Through $O(\alpha_S^4)$,
Phys. Rev. Lett. **110** (2013) 252004, arXiv: 1303.6254 [hep-ph] (cit. on p. 6).

[61] M. Czakon and A. Mitov,
Top++: A program for the calculation of the top-pair cross-section at hadron colliders,
Comput. Phys. Commun. **185** (2014) 2930, arXiv: 1112.5675 [hep-ph] (cit. on p. 6).

[62] N. Kidonakis,
Two-loop soft anomalous dimensions for single top quark associated production with a W^- or H^-,
Phys. Rev. D **82** (2010) 054018, arXiv: 1005.4451 [hep-ph] (cit. on p. 6).

[63] N. Kidonakis, 'Top Quark Production', *Proceedings, Helmholtz International Summer School on Physics of Heavy Quarks and Hadrons (HQ 2013)* (JINR, Dubna, Russia, 15th–28th July 2013) 139, arXiv: 1311.0283 [hep-ph] (cit. on p. 6).

[64] C. Anastasiou, L. Dixon, K. Melnikov and F. Petriello, *High-precision QCD at hadron colliders: Electroweak gauge boson rapidity distributions at next-to-next-to leading order*,
Phys. Rev. D **69** (2004) 094008, arXiv: hep-ph/0312266 (cit. on p. 6).

[65] D. J. Lange, *The EvtGen particle decay simulation package*,
Nucl. Instrum. Meth. A **462** (2001) 152 (cit. on p. 6).

[66] ATLAS Collaboration, *The Pythia 8 A3 tune description of ATLAS minimum bias and inelastic measurements incorporating the Donnachie–Landshoff diffractive model*,
ATL-PHYS-PUB-2016-017, 2016, URL: https://cds.cern.ch/record/2206965
(cit. on p. 6).

[67] M. Grazzini, S. Kallweit, D. Rathlev and M. Wiesemann,
$W^{\pm}Z$ production at hadron colliders in NNLO QCD, Phys. Lett. B **761** (2016) 179,
arXiv: 1604.08576 [hep-ph] (cit. on p. 5).

[68] M. Grazzini, S. Kallweit, D. Rathlev and M. Wiesemann,
$W^{\pm}Z$ production at the LHC: fiducial cross sections and distributions in NNLO QCD,
JHEP **05** (2017) 139, arXiv: 1703.09065 [hep-ph] (cit. on p. 5).

[69] M. Grazzini, S. Kallweit and D. Rathlev,
ZZ production at the LHC: Fiducial cross sections and distributions in NNLO QCD,
Phys. Lett. B **750** (2015) 407, arXiv: 1507.06257 [hep-ph] (cit. on p. 5).

[70] F. Cascioli et al., *ZZ production at hadron colliders in NNLO QCD*, Phys. Lett. B **735** (2014) 311,
arXiv: 1405.2219 [hep-ph] (cit. on p. 5).

[71] M. Grazzini, S. Kallweit, S. Pozzorini, D. Rathlev and M. Wiesemann,
W^+W^- production at the LHC: fiducial cross sections and distributions in NNLO QCD,
JHEP **08** (2016) 140, arXiv: 1605.02716 [hep-ph] (cit. on pp. 5, 19).

[72] ATLAS Collaboration, *Performance of electron and photon triggers in ATLAS during LHC Run 2*,
Eur. Phys. J. C **80** (2020) 47, arXiv: 1909.00761 [hep-ex] (cit. on pp. 6, 17).

[73] ATLAS Collaboration, *Performance of the ATLAS muon triggers in Run 2*,
JINST **15** (2020) P09015, arXiv: 2004.13447 [hep-ex] (cit. on pp. 6, 17).

[74] ATLAS Collaboration, *Electron reconstruction and identification in the ATLAS experiment using the 2015 and 2016 LHC proton–proton collision data at $\sqrt{s} = 13$ TeV*,
Eur. Phys. J. C **79** (2019) 639, arXiv: 1902.04655 [hep-ex] (cit. on p. 6).

[75] ATLAS Collaboration, *Electron and photon performance measurements with the ATLAS detector using the 2015–2017 LHC proton–proton collision data*, JINST **14** (2019) P12006,
arXiv: 1908.00005 [hep-ex] (cit. on pp. 6, 7, 17).

[76] ATLAS Collaboration, *Muon reconstruction and identification efficiency in ATLAS using the full Run 2 pp collision data set at $\sqrt{s} = 13$ TeV*, Eur. Phys. J. C **81** (2021) 578,
arXiv: 2012.00578 [hep-ex] (cit. on pp. 7, 17).

[77] ATLAS Collaboration, *Muon reconstruction performance of the ATLAS detector in proton–proton collision data at $\sqrt{s} = 13$ TeV*, Eur. Phys. J. C **76** (2016) 292, arXiv: 1603.05598 [hep-ex]
(cit. on p. 7).

[78] M. Cacciari, G. P. Salam and G. Soyez, *The anti-k_t jet clustering algorithm*, JHEP **04** (2008) 063,
arXiv: 0802.1189 [hep-ph] (cit. on p. 7).

[79] ATLAS Collaboration,
Jet reconstruction and performance using particle flow with the ATLAS Detector,
Eur. Phys. J. C **77** (2017) 466, arXiv: 1703.10485 [hep-ex] (cit. on p. 7).

[80] ATLAS Collaboration, *Performance of pile-up mitigation techniques for jets in pp collisions at $\sqrt{s} = 8$ TeV using the ATLAS detector*, Eur. Phys. J. C **76** (2016) 581,
arXiv: 1510.03823 [hep-ex] (cit. on p. 7).

[81] ATLAS Collaboration, *Jet energy scale and resolution measured in proton–proton collisions at $\sqrt{s} = 13$ TeV with the ATLAS detector*, Eur. Phys. J. C **81** (2020) 689,
arXiv: 2007.02645 [hep-ex] (cit. on pp. 7, 17).

[82] ATLAS Collaboration, *Optimisation and performance studies of the ATLAS b-tagging algorithms for the 2017-18 LHC run*, ATL-PHYS-PUB-2017-013, 2017, URL: https://cds.cern.ch/record/2273281 (cit. on p. 7).

[83] ATLAS Collaboration, *ATLAS b-jet identification performance and efficiency measurement with $t\bar{t}$ events in pp collisions at $\sqrt{s}$ = 13 TeV*, Eur. Phys. J. C **79** (2019) 970, arXiv: 1907.05120 [hep-ex] (cit. on pp. 7, 17).

[84] ATLAS Collaboration, *Performance of missing transverse momentum reconstruction with the ATLAS detector using proton–proton collisions at $\sqrt{s}$ = 13 TeV*, Eur. Phys. J. C **78** (2018) 903, arXiv: 1802.08168 [hep-ex] (cit. on p. 7).

[85] ATLAS Collaboration, *Measurement of the $t\bar{t}$ production cross-section and lepton differential distributions in $e\mu$ dilepton events from pp collisions at $\sqrt{s}$ = 13 TeV with the ATLAS detector*, Eur. Phys. J. C **80** (2020) 528, arXiv: 1910.08819 [hep-ex] (cit. on p. 8).

[86] ATLAS Collaboration, *Measurement of $W^{\pm}$ and Z-boson production cross sections in pp collisions at $\sqrt{s}$ = 13 TeV with the ATLAS detector*, Phys. Lett. B **759** (2016) 601, arXiv: 1603.09222 [hep-ex] (cit. on p. 12).

[87] ATLAS Collaboration, *Measurement of $W^{\pm}Z$ production cross sections and gauge boson polarisation in pp collisions at $\sqrt{s}$ = 13 TeV with the ATLAS detector*, Eur. Phys. J. C **79** (2019) 535, arXiv: 1902.05759 [hep-ex] (cit. on p. 12).

[88] ATLAS Collaboration, *Multi-boson simulation for 13 TeV ATLAS analyses*, ATL-PHYS-PUB-2016-002, 2016, URL: https://cds.cern.ch/record/2119986 (cit. on p. 12).

[89] M. Grazzini, S. Kallweit and D. Rathlev, *$W\gamma$ and $Z\gamma$ production at the LHC in NNLO QCD*, JHEP **07** (2015) 085, arXiv: 1504.01330 [hep-ph] (cit. on p. 12).

[90] M. Cacciari and G. P. Salam, *Pileup subtraction using jet areas*, Phys. Lett. B **659** (2008) 119, arXiv: 0707.1378 [hep-ph] (cit. on p. 16).

[91] W. Verkerke and D. P. Kirkby, *The RooFit toolkit for data modeling*, eConf **C0303241** (2003) MOLT007, ed. by L. Lyons and M. Karagoz, arXiv: physics/0306116 (cit. on p. 16).

[92] G. D'Agostini, *A multidimensional unfolding method based on Bayes' theorem*, Nucl. Instr. Meth. A **362** (1995) 487 (cit. on pp. 3, 16).

[93] G. D'Agostini, *Improved iterative Bayesian unfolding*, (2010), arXiv: 1010.0632 [physics.data-an] (cit. on pp. 3, 16).

[94] ATLAS Collaboration, *Studies of the muon momentum calibration and performance of the ATLAS detector with pp collisions at $\sqrt{s}$ = 13 TeV*, (2022), arXiv: 2212.07338 [hep-ex] (cit. on p. 17).

[95] ATLAS Collaboration, *Study of top-quark pair modelling and uncertainties using ATLAS measurements at $\sqrt{s}$ = 13 TeV*, ATL-PHYS-PUB-2020-023, 2020, URL: https://cds.cern.ch/record/2730443 (cit. on p. 17).

[96] M. Grazzini, S. Kallweit, J. M. Lindert, S. Pozzorini and M. Wiesemann, *NNLO QCD + NLO EW with Matrix+OpenLoops: precise predictions for vector-boson pair production*, JHEP **02** (2020) 087, arXiv: 1912.00068 [hep-ph] (cit. on p. 19).

[97] M. Grazzini, S. Kallweit, M. Wiesemann and J. Y. Yook,
W^+W^- production at the LHC: NLO QCD corrections to the loop-induced gluon fusion channel,
Phys. Lett. **B804** (2020) 135399, arXiv: 2002.01877 [hep-ph] (cit. on pp. 19, 27).

[98] T. Gehrmann et al.,
W^+W^- Production at Hadron Colliders in Next to Next to Leading Order QCD,
Phys. Rev. Lett. **113** (2014) 212001, arXiv: 1408.5243 [hep-ph] (cit. on p. 19).

[99] M. Grazzini, S. Kallweit and M. Wiesemann, *Fully differential NNLO computations with MATRIX*,
(2017), arXiv: 1711.06631 [hep-ph] (cit. on p. 19).

[100] A. von Manteuffel and L. Tancredi, *The two-loop helicity amplitudes for $gg \to V_1V_2 \to 4$ leptons*,
JHEP **06** (2015) 197, arXiv: 1503.08835 [hep-ph] (cit. on p. 19).

[101] T. Gehrmann, A. von Manteuffel and L. Tancredi,
The two-loop helicity amplitudes for $q\overline{q}' \to V_1V_2 \to 4$ leptons, JHEP **09** (2015) 128,
arXiv: 1503.04812 [hep-ph] (cit. on p. 19).

[102] F. Buccioni et al., *OpenLoops 2*, Eur. Phys. J. C **79** (2019) 866, arXiv: 1907.13071 [hep-ph]
(cit. on pp. 19, 20).

[103] F. Buccioni, S. Pozzorini and M. Zoller, *On-the-fly reduction of open loops*,
Eur. Phys. J. C **78** (2018) 70, arXiv: 1710.11452 [hep-ph] (cit. on p. 19).

[104] S. Catani, L. Cieri, D. de Florian, G. Ferrera and M. Grazzini,
Vector boson production at hadron colliders: hard-collinear coefficients at the NNLO,
Eur. Phys. J. **C72** (2012) 2195, arXiv: 1209.0158 [hep-ph] (cit. on p. 19).

[105] S. Catani and M. Grazzini, *Next-to-Next-to-Leading-Order Subtraction Formalism in Hadron Collisions and its Application to Higgs-boson Production at the Large Hadron Collider*,
Phys. Rev. Lett. **98** (2007) 222002, arXiv: hep-ph/0703012 [hep-ph] (cit. on p. 19).

[106] R. D. Ball et al., *Parton distributions from high-precision collider data*,
Eur. Phys. J. C **77** (2017) 663, arXiv: 1706.00428 [hep-ph] (cit. on pp. 19, 27).

[107] V. Bertone, S. Carrazza, N. P. Hartland and J. Rojo,
Illuminating the photon content of the proton within a global PDF analysis,
SciPost Phys. **5** (2018) 008, arXiv: 1712.07053 [hep-ph] (cit. on pp. 19, 27).

[108] M. Grazzini, S. Kallweit, J. M. Lindert, S. Pozzorini and M. Wiesemann, *NNLO QCD + NLO EW with Matrix+OpenLoops: precise predictions for vector-boson pair production*,
JHEP **02** (2020) 087, arXiv: 1912.00068 [hep-ph] (cit. on pp. 19, 22, 23, 27, 37).

Appendix

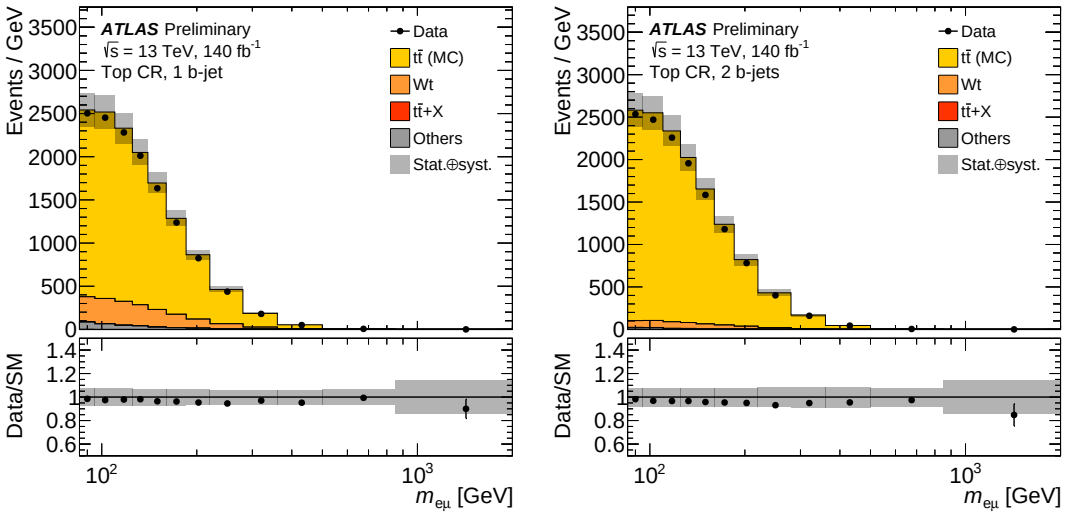

(a) (b)

Figure 13: Comparison of data and simulation in bins of $m_{e\mu}$ in the $t\bar{t}$ control regions with (a) 1 b-jet and (b) 2 b-jets. Data are shown as black markers, together with histograms for the predictions of signal and background processes. The rightmost bin contains overflow events. The lower panels show the ratio of the data to the total prediction. The uncertainty bands shown include statistical and systematic uncertainties.

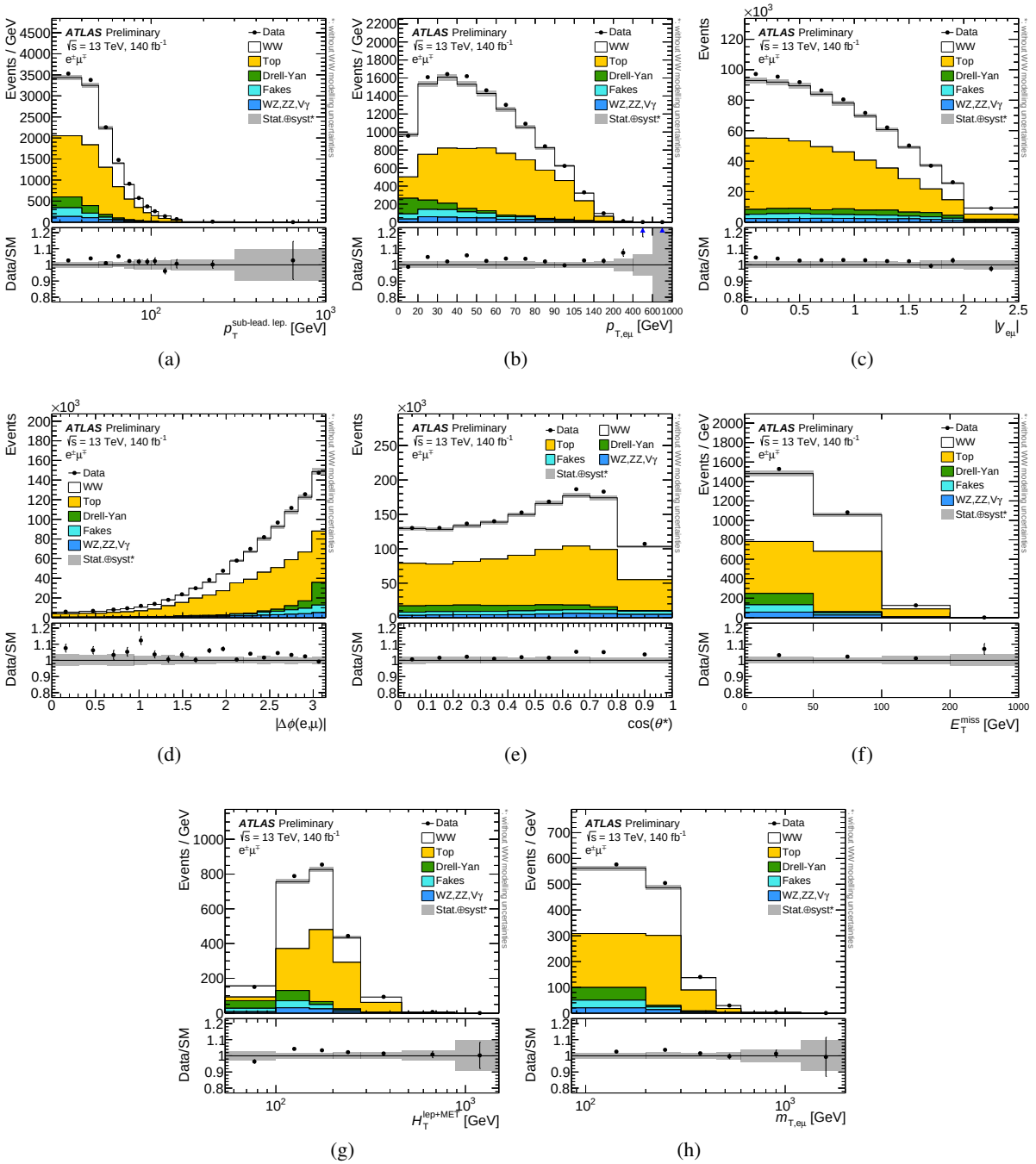

Figure 14: (a) $p_{\mathrm{T}}^{\text{sub-lead. lep.}}$, (b) $p_{\mathrm{T},e\mu}$ (c) $y_{e\mu}$, (d) $|\Delta\phi_{e\mu}|$, (e) $|\cos\theta^{*}|$, (f) $E_{\mathrm{T}}^{\mathrm{miss}}$, (g) $H_{\mathrm{T}}^{\text{lep.+MET}}$ and (h) $m_{\mathrm{T},e\mu}$ distributions at detector level, for the signal region event selection. Data are shown as black markers together with histograms for the predictions of signal and background processes. The rightmost bin contains overflow events. The lower panels show the ratio of the data to the total prediction. Top and fake backgrounds are determined using data-driven methods. The uncertainty bands shown include statistical and systematic uncertainties, excluding theory uncertainties on the signal, which largely cancel in the measurement of WW cross-sections.

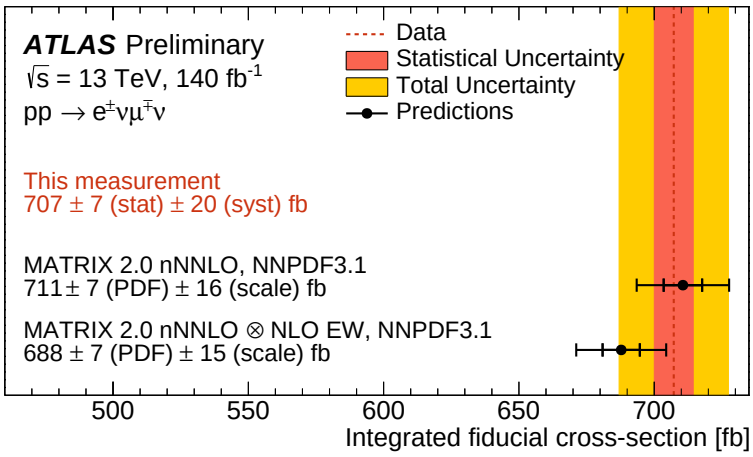

Figure 15: Measured fiducial fiducial cross-sections, compared to a theoretical predictions from MATRIX+OpenLoops [108]. The theoretical predictions use the NNPDF3.1nnlo luxQED set of parton distribution functions, are of NNLO accuracy in QCD for $q\bar{q} \to WW$ production and include NLO QCD corrections to $gg \to WW$ production, which constitute part of the N^{3}LO correction, as well as photon induced contributions. One prediction is combined multiplicatively with NLO EW corrections to $q\bar{q} \to WW$. The inner (outer) error bars on the theory prediction includes PDF uncertainties (PDF and scale uncertainties added in quadrature).